Abstract

DI JULIO, DOUGLAS DAVID. A Gd Based Gaseous Electron Multiplier Detector for Neutron Scattering Applications. (Under the direction of Ayman I. Hawari.)

The Gaseous Electron Multiplier (GEM) neutron detector is one of several new concepts that are being designed for the next generation neutron sources. The detector contains multiple modules where each module contains a central neutron converter, several cascaded GEM foils, and readout plates on both sides of the cathode. The device employs a Gd/CsI converter sandwich to convert the neutron to an electric signal. Upon neutron absorption in the Gd layer, conversion electrons are emitted with a probability of 86.5%. Primary electrons travel into the CsI and multiply, inducing the emission of low energy electrons from the converter surface. Several cascaded GEM foils placed on both sides of the converter amplify the signal. The position of the signal is then time stamped and detected by position sensitive anodes and localization electronics.

Extensive Monte Carlo simulations, using the PENELOPE code package, have been completed in order to calculate integral and differential characteristics (i. e. the average number of secondary electrons emitted from the converter and the secondary electron escape probability distribution) of various converter thicknesses. The performance of the detector can be assessed by estimating the secondary electron (SE) leakage from the converter foil. Simulations to calculate the SE leakage have been performed for both the single and several multiple module designs. The multiple module design allows for a greater SE leakage while maintaining high detector efficiency and divides the total count rate among several sets of decoding electronics.

Tests of several different detector prototypes were completed at the NCSU PULSTAR reactor. Results of the tests of the prototype detectors revealed the essential

elements of detector operation. Detector efficiencies, pulse height spectra, and 2-D position spectra have been measured with each of the detector prototypes.

A Gd Based Gaseous Electron Multiplier Detector for Neutron Scattering Applications

by
Douglas David Di Julio II

A thesis submitted to the Graduate Faculty of
North Carolina State University
in partial fulfillment of the
requirements for the Degree of
Master of Science

NUCLEAR ENGINEERING

Raleigh, North Carolina

2007

Approved by:

_____	_____
Dr. Ayman I. Hawari Chair of Advisory Committee	Dr. Pierre A. Gremaud
_____	_____
Dr. Mohamed A. Bourham	Dr. Ronald R. Berliner

Biography

Douglas David Di Julio II was born in Bellevue, Washington to Douglas and Regina Di Julio. He grew up in the town of Mercer Island, Washington, just outside the city of Seattle.

In June of 2001, the author graduated from Mercer Island High School and that following fall he began attending the University of Washington located in Seattle. In the spring of 2005 the author received his Bachelor of Science in Physics with a minor in Swedish.

The author began graduate studies in nuclear engineering at North Carolina State University under the supervision of Dr. Ayman Hawari in July of 2005.

Acknowledgements

The author would like to thank Dr. Ayman Hawari for his continuous guidance and support throughout the course of this project, without which, none of this would have been possible.

The author would also like to extend his gratitude to Dr. Ronald R. Berliner. His guidance and advice provide lessons that cannot be learned just anywhere. Undoubtedly these lessons will be invaluable in the future.

Thanks should also be given to Dr. Tong Zhou for both his patience and for providing assistance and advice throughout several different stages of the project. The thanks should also be extended to Iyad Al-Qasir, Brian Hehr, Jason Harp, and Kenny Anderson.

The author would also like to thank Mr. Andrew Cook, Mr. Larry Broussard, Mr. Kerry Kincaid, Mr Gerald Wicks, and the rest of the staff at the NCSU PULSTAR reactor for their continuous assistance during the testing of the GEM neutron detectors.

Finally, the author would like to thank his family for their continuous support throughout all stages of his education. These include his father Doug Di Julio, his mother Regina Di Julio, his brother Ross Di Julio, and his two sisters Jessica and Rebecca Di Julio. His gratitude also extends to his grandparents for their words of encouragement over the past many years. Lastly, the author would like to thank Anna Preger, whom resides in Sweden, for her infinite patience and suggestions.

Support for this work was provided by Instrumentation Associates under a DOE Phase-II SBIR, “A GEM of a Neutron Detector”, DE-FG02-03ER83685.

Table of Contents

List of Tables

List of Figures

Chapter 1 Introduction

1.1 Introduction to Neutron Scattering

Neutron scattering methods provide basic information on the structure and dynamics of materials in many different fields of science. Several properties of the neutron make it a unique candidate for the study of materials on the atomic and molecular scale. Neutrons have no charge and interact with atoms via very short-range nuclear forces (~1 fermi). The distance between scattering centers (nucleus) is about 100,000 times larger than the scattering center itself [1]. Due to these properties, the neutron can penetrate deep into the bulk of materials. This is in contrast to other possible probes of atomic structure. X-rays are scattered by electrons in an atom. Therefore, light materials do not scatter x-rays as effectively as heavy materials. Electrons also suffer from the same problem as x-rays. Electrons have electrostatic interactions in the material and are unsuitable for examining the inside of bulk materials [1]. The various probes of matter on the atomic level and their interactions in a material are shown in Fig. 1.1.

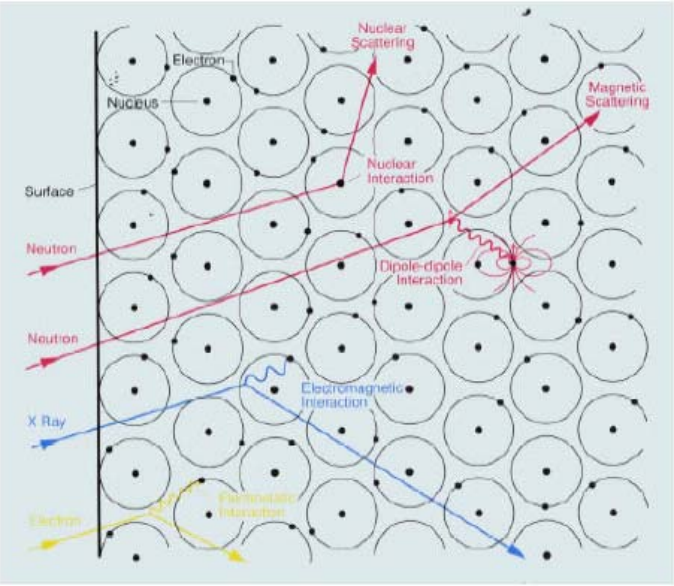

Figure 1.1: Various probes of matter on the atomic level and their interactions [1].

In addition to the above properties, the wavelength of thermal neutrons is comparable to interatomic distances, and the energy is similar to the energy of excitations in condensed matter. This makes the neutron well suited for studying low energy excitations such as lattice vibrations in materials.

Magnetism on the atomic scale can also be studied by exploiting the neutrons magnetic moment. Neutrons behave as tiny magnets, and interact with the unpaired electrons in materials. It is therefore possible to study magnetic structures and excitations in material.

Along with the above-mentioned advantages of using the neutron for scattering experiments, there are several disadvantages. Beam intensities at this current time are magnitudes of order smaller than those for x-rays. Fortunately, with the upcoming next generation neutron sources, new heights in neutron beam intensities will be reached. Along with this increase in neutron beam intensity comes the need to develop better detector technology, which is capable of handling the new count rates.

1.2 Neutron Production

Neutrons used for scattering experiments can be generated by either a continuous source (e.g., a nuclear reactor) or a pulsed source (e.g., a spallation neutron source). The evolution of neutron sources over the last several decades is shown in Fig. 1.2. The energies of the neutrons produced have very high energies and must be reduced in energy (to thermal or sub-thermal energies) before being used for neutron scattering experiments. A moderating material, with a very high neutron scattering cross-section, is used to achieve this end. The neutrons enter the moderator, which is placed close to the source, and undergo many collisions. The emerging neutron distribution will be Maxwellian, and will have an average speed determined by the temperature of the moderator.

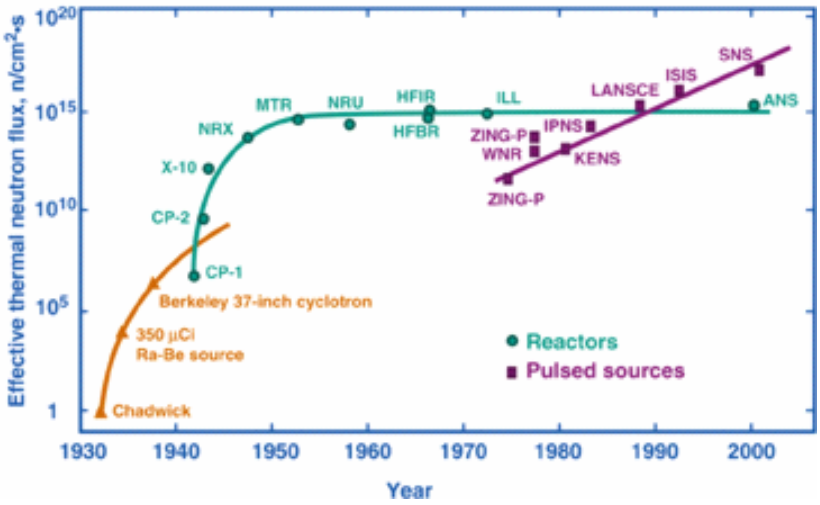

Figure 1.2: The Evolution of neutron sources [2].

A continuous source, such as a reactor, produces neutrons, which arise from the spontaneous fission of a fuel such as ^{235}U. The emerging neutrons from the moderator usually need to be collimated and then monochromated. Bragg reflection from a single crystal monochromator leads to the selection of a narrow energy band of neutrons. It is then possible to vary the wavelength of the neutrons by varying the angle at the monochromator. The current generation of neutron reactor sources has reached a plateau in source strength at about $1\times10^{15}\ \frac{neutrons}{cm^2}$.

Spallation sources on the other hand produce neutrons by bombarding a heavy target with high-energy protons. Several target possibilities are U, W, and Hg. The neutrons from such a pulsed source are generated in bursts of particles. All neutrons produced at a spallation source can be used as oppose to the continuous source case discussed above. It is possible to calculate the neutron wavelength by the time-of-flight (TOF) method. Next generation neutron sources, such as the Spallation Neutron Source (SNS), will have a peak flux that will be much higher than current reactor sources. Table 1.1 shows several of the characteristics of current and next generation neutron sources.

Table 1.1: Current and Next Generation neutron sources [3].

Source	Reaction Type	Target Type	Pulse Frequency (Hz)	Protons per pulse	Peak nth flux per pulse (v cm^{-2})[a]	Peak nth flux per pulse normalized to ISIS	Average nth flux ($cm^{-2}s^{-1}$)
ILL	Reactor	-	Continuous	-	-	-	1.2×10^{15}
ISIS	Pulsed	Ta	50	2.5×10^{13}	4.6×10^{13}	1	2×10^{12}
SNS	Pulsed	Hg	60	1.5×10^{14}	1×10^{15}	~20	8×10^{13}

[a]The peak nth flux per pulse is normalized to v, the pulse frequency.

1.3 Neutron Detection and Measurement

Since neutrons are not directly ionizing they must be detected through nuclear reactions that produce ionizing radiation (e.g., charged particles, gamma-rays, etc.). Most neutron detectors use a specific material for this conversion process, which is followed by conventional radiation detector methods. Depending on the energy range of interest, different types of materials are used for neutron conversion. Slow neutrons, by convention, are considered those with energy less than the cadmium cutoff of 0.5 eV. The application of the neutron detector being built in this paper will be used to detect thermal neutrons (about 0.0253 eV). Hence the rest of this paper will be concerned with only slow neutron detection methods.

There are several important characteristics when choosing an appropriate neutron converter. The material must have a large absorption cross-section for the energy range of interest. It is also important that the energy given to the reaction products (Q-value) be large. A large Q-value ensures that the reaction products will have greater energy, making it easier to discriminate from signals that may arise due gamma-ray events that often accompany neutrons [4].

In order to further discriminate against low amplitude signals that may arise from noise, it is important to try to capture as much of the reaction products energy within the

volume of the detector. If the detector uses a gas to convert the neutrons, this requirement imposes severe restrictions on the type of material and size of the detector. This is due to the fact that the ranges of the typical conversion products are on the order of centimeters in a gas [4]. Neutron reaction products that do not lose all their energy within the volume of the detector lead to low-amplitude signals that will deteriorate the performance of the detector.

1.4 Nuclear Reactions

The cross-section as a function of the neutron energy is shown in Fig. 1.3 and several of the popular neutron converter reactions are listed in Table 1.2. The cross-section for thermal neutrons along with the Q-value and the reaction type are listed. Most of the reactions listed in the table lead to the emission of heavy charged particles, however, the ^{nat}Gd and ^{157}Gd neutron capture reactions lead to the emission of conversion electrons. Several of the reactions listed in the table will be discussed in detail below.

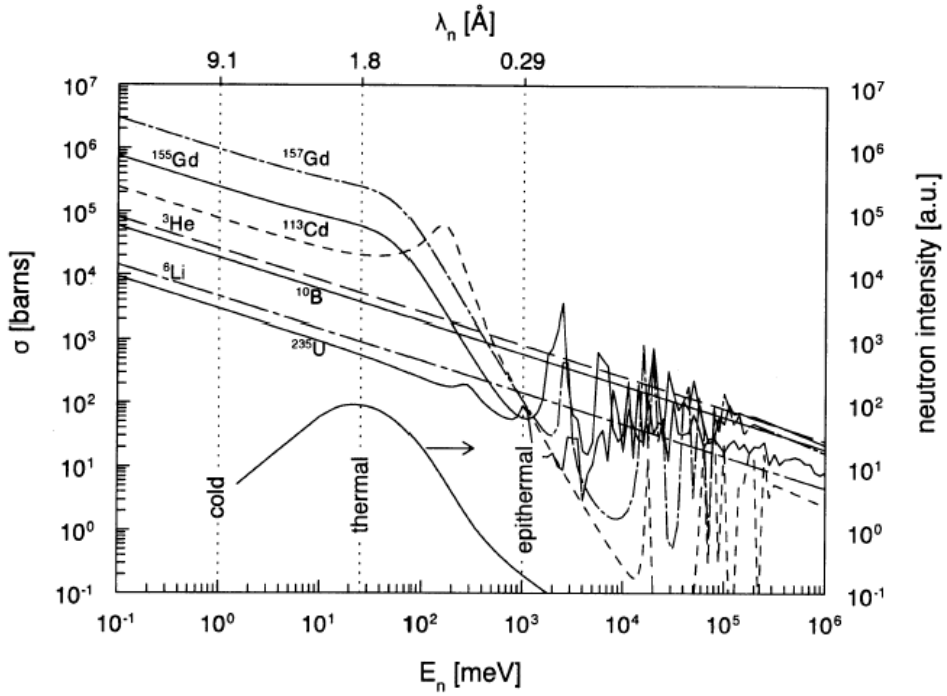

Figure 1.3: Cross-section as a function of Energy for various reactions [7].

Table 1.2: Neutron Converters and Cross-sections [5][4].

Isotope	Reaction	Q Value (MeV)	Cross-Section (barn)
^{3}He	^{3}He(n, p)t	0.764	5333
^{10}B	^{10}B(n,α)^{7}Li (6%)	2.792	3836
	^{10}B(n,α)^{7}Li* (94%)	2.310	
^{6}Li	^{6}Li(n,α)t	4.78	940
^{Nat}Gd	^{Nat}Gd(n,γ)	0.029 – 0.182[a]	49,700[b]
^{157}Gd	^{157}Gd(n,γ)^{158}Gd	0.029 – 0.182 [a]	255,000

[a]Conversion electrons, [b]ILL [6]

1.4.1 The ^{3}He(n, p)t Reaction

The ^{3}He(n, p)t reaction is probably the most commonly employed reaction when detecting neutrons. The cross-section for ^{3}He is quite high, 5333 b for thermal neutrons and varies as 1/v. However, the relatively small Q value of the reaction makes gamma ray discrimination a little worse than with other reactions under consideration.

Proportional counters filled with ^{3}He gas are a widely used type of detector. These types of detectors exhibit a high neutron detection efficiency (nearly 100%) however they can suffer from the wall effect. If a reaction occurs closely to the wall of the detector, some events may not deposit the full reaction energy into the gas. This leads to small amplitude signals that add a small continuum of pulses to the pulse height spectrum. There are several methods for reducing this effect. The diameter of the detector can be increased [4]. Also the stopping power of the gas can be increased by increasing the pressure of the gas or by adding a fraction of another gas with higher stopping power [4]. This however leads to extended signal duration time and higher gamma sensitivity [8]. For time-of-flight (TOF) measurements, it is important to have a fast rise time.

A typical example of a position sensitive ^{3}He proportional tube is shown in Fig. 1.4. The metal tube in the figure is filled with ^{3}He gas. Electrons due to ionization in the fill gas by the reaction products are accelerated to the anode by the detector bias. The positive ions are then drifted towards the cathode resulting in an equal but opposite charge being deposited on the anode and cathode [9].

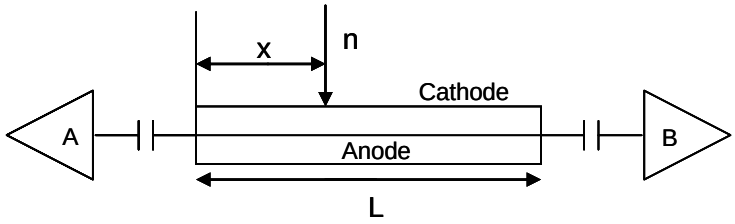

Figure 1.4: ^{3}He proportional counter

The current at position x, induced by the injection of a charge, divides into two which flow to the left and right through the anode resistance. By knowing the charge that passes through the A and B side preamplifiers it is possible to calculate the position of the neutron absorption by the charge division method.

1.4.2 The $^{10}B(n,\alpha)^{7}Li$ Reaction

The $^{10}B(n,\alpha)^{7}Li$ is also a popular reaction choice when designing a neutron detector. ^{10}B has a cross-section of 3836 b, which is relatively high, but lower than that of ^{3}He. The cross-section is also a 1/v type. ^{10}B can also be used in either gaseous form, such as a BF_3 counter or in a solid form.

The BF_3 proportional counter is usually enriched with 90% ^{10}B [8]. The counter detects both of the ions resulting from the reaction. Depending on the size of the counter, the wall effect can be observed. Detectors of this type can easily discriminate against gamma rays. The neutron reaction products produce much larger ionization in the gas than the electrons resulting from gamma ray ionization. Amplitude discrimination can then be used to

remove this noise [10]. However, in intense gamma fields, the pileup of gammas can be a problem [10].

Detectors employing solid ^{10}B as a converter have also been used for neutron detection. However, due to the short range of the reaction products in a solid, these detectors are limited in their efficiency.

1.4.3 The $^{6}Li(n,\alpha)t$ Reaction

The cross-section of the $^{6}Li(n,\alpha)t$ reaction, 940 b, is rather low when compared to the above reactions. This is however slightly offset by the large Q value of the reaction products. Lithium can be used as a solid, as the component of a scintillator, or in the form of LiF.

1.4.4 The $^{nat}Gd(n,\gamma)$ Reaction

Gadolinium is an attractive converter material because of its high neutron absorption cross-section for thermal neutrons (49,700 barns for natural Gd at a neutron energy of 0.0253 eV). When a neutron is captured by a Gd nucleus, conversion electrons are emitted with a probability of 86.5% and an energy in the range of 29 keV to 180 keV [7]. Along with the emission of conversion electrons, several high-energy gamma rays are also released. Due to this and the low reaction Q value, a means for the discrimination of gamma rays will be necessary if this converter is to be employed. The usage of isotopically enriched Gd would increase the thermal neutron absorption efficiency of the detector.

1.5 Detectors and Instruments at the Next Generation Neutron Sources

Due to the increase of almost a factor of 20 (Table 1.1) in the peak neutron flux at the SNS when compared to today's currently most intense source, higher requirements on detectors will be demanded by neutron scattering instruments. This will be slightly offset by investigating smaller samples due to the increase in flux [3].

Many instruments' efficiency will severely depend on the performance of the detectors. Table 1.3 shows desired characteristics of two such instruments at the SNS, the magnetism reflectometer and the liquids reflectometer.

Table 1.3: Comparisons of current and desired characteristics for two instruments at the SNS [11].

Instrument	Pixel Area (cm^2)	Number of pixels	Neutron capture efficiency	Max neutron energy (eV)	Time Resolution (μs)	Peak pixel count rate (n/s)	Detector count rate (n/s)[a]
Liquids	0.01	40,000	50%	0.02	10	1×10^6	7×10^7
Magnetism	0.02	40,000	50%	0.03	10	1×10^6	9×10^7

[a]Rate for entire system.

High angle diffraction of magnetic thin films is a typical example of an area that would be studied with a magnetism reflectometer [12]. The liquids reflectometer will be useful in interfacial studies in polymers [13]. Fig. 1.5 shows a diagram of the magnetism reflectometer that was built at the SNS.

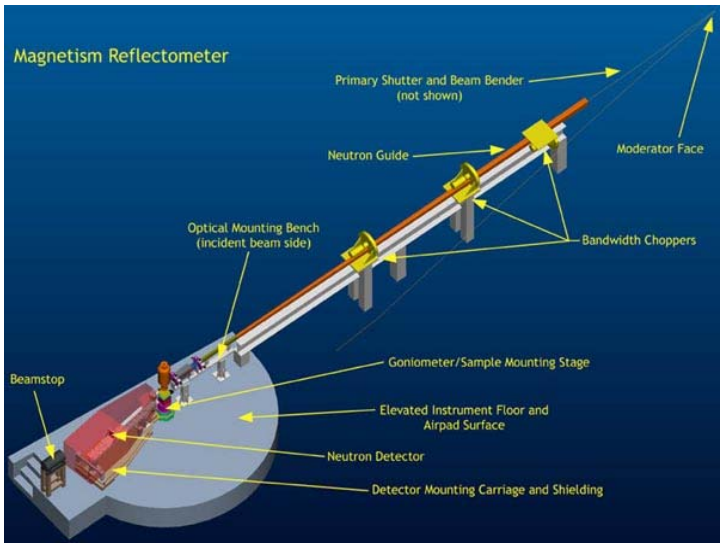

Figure 1.5: The magnetism reflectometer at the SNS [12].

As an example, a ^{3}He proportional counter similar to the one discussed above will be compared to these requirements. ^{3}He proportional counters are also one of the most commonly used detectors at a reflectometer [11].

For 0.0253 eV neutrons the neutron absorption length is 7.59 bar cm in pure ^{3}He gas. Due to this, the detector will need to operate under pressures of about 10 bars if 100% neutron efficiency is desired. This leads to the creation of a detector with safety concerns and a large entrance window thickness. This will lead to unwanted neutron absorption and scattering, which will have an effect on the measurements. Since conversion of the neutron can take place anywhere in the gas, the TOF resolution is limited by the thickness of the converter. Typically detectors of 1-3 cm are needed for acceptable neutron absorption efficiency. For the above thicknesses the neutron transit time across the converter is between 4.5 μs – 13.6 μs.

Even though ^{3}He proportional counters demonstrate characteristics that are adequate for most reactor experiments, at the next generation neutron sources they will saturate at 1% of the max rate [11]. An improvement in detector technology will greatly increase the efficiency of these instruments at next generation neutron sources.

Chapter 2 Design of the GEM Neutron Detector

2.1 Overview of the GEM Detector Design

A Gd based Gaseous Electron Multiplier [14] neutron detector is being designed to meet several of the requirements put forth by next generation neutron sources. Fig. 2.1 shows the conceptual design for a single module of the detector.

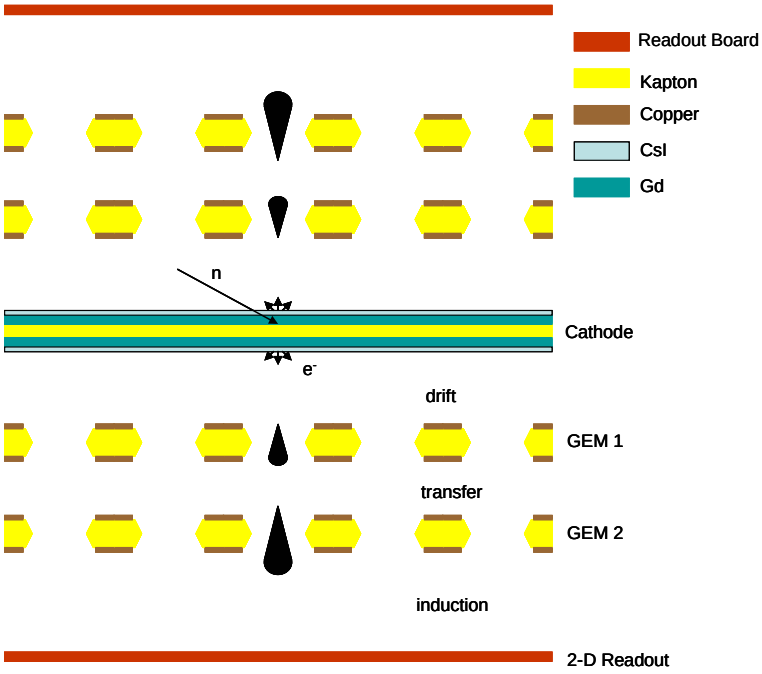

Figure 2.1: Conceptual design of the GEM neutron detector.

The detector is comprised of multiple detector modules. The central element to a module is the Gd-CsI sandwich [15]. Gd is evaporated onto both side of a thin foil of kapton and covered with a layer of CsI. Neutrons, which are captured in the Gd, lead to the emission of primary electrons. These primary electrons travel into the CsI and multiply creating secondary electrons. The cloud of secondary electrons, localized around the position of neutron absorption, which escape the surface of the CsI serve as the primary source of ionization in the fill gas. Ionization produced by the secondary electrons then undergoes two levels of amplification before the position of the cloud is detected on a 2-D readout board.

Sub-millimeter position sensing along with excellent time of flight resolution is expected with the detector. Along with the possibly of high data rate, low fabrication cost, high efficiency, and possibility of a large sensitive area, the GEM detector is a candidate for neutron scattering applications at next generation neutron sources.

2.2 The Neutron Converter Sandwich

Solid neutron converter foils have several advantages over gaseous neutron converter foils. By using thin solid foils, it ensures that any neutron absorption will occur within the thickness of the foil, which leads to excellent TOF resolution. A thickness of about 1 cm is required for sufficient neutron absorption in a gas converter, which leads a thermal neutron transit time of 4.5 μs. In a solid converter, a thickness of several micrometers is needed, which means that the conversation gap is much smaller. Therefore, higher TOF resolution is expected with a solid converter.

The neutron converter used in the GEM detector is a CsI-Gd-Kapton-Gd-CsI sandwich. A 7.5 μm kapton foil forms the mechanical support for the Gd and CsI layers. Neutron absorption in the ^{nat}Gd layers results in primary electron emission about 86.5% of the time [7]. Table 2.1 shows the energy spectrum of these emitted electrons for a single neutron captured in the Gd.

Table 2.1: Gd Conversion Spectrum relative to a neutron capture [16].

Energy (keV)	Relative Frequency
29	0.299
71	0.498
78	0.122
131	0.056
174	0.02
180	0.005

The interaction of the primary electrons within the CsI induces a cascade of interactions, which leads to low energy secondary electron emission. CsI is an excellent candidate for secondary electron emission. This is mainly due to its low work function of 0.1 – 0.2 eV [15]. Low energy electrons also have a relatively long mean free path in the solid [17]. These low energy electrons released from the CsI are well localized around the location of neutron absorption within the Gd [18]. Secondary electron emission from CsI will be discussed in further detail in the next chapter.

2.3 GEM Foils

Sauli at CERN developed the GEM foil in 1997 [14]. The GEM is a kapton foil that is copper coated on both sides and pierced electrochemically with a high-density array of micrometer sized holes as seen in Fig. 2.2. By applying a potential of several hundred volts between the metal layers, shown in Fig. 2.3, electrons in the gas above the foil are drifted into the holes where gas multiplication and electron gain occur. Gains in excess of 10^3 have been achieved with a single GEM and even higher gains can be reached by using multiple GEM structures in series [19]. GEM detectors have also demonstrated excellent localization accuracy and high data rate capability [20].

GEM amplifiers can also be cascaded together so that the amplification is shared between separate GEM stages. The stability of the GEM foils also increases in this mode of operation since the GEM foils can operate at lower voltages.

The kapton in the GEM foils is 0.051 mm coated with 5 μm of copper on both sides. The profile of the holes is double conical, with the narrower diameter in the center of the holes. The copper diameter is 0.076 mm and the diameter in the center of the kapton is 0.051

mm. The holes are arranged in a hexagonal pattern with a distance of 0.140 mm between the holes.

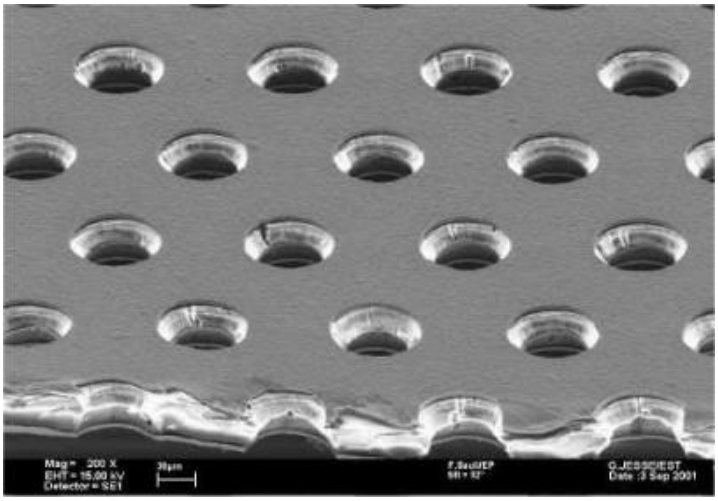

Figure 2.2: Photograph of the GEM foil surface [21].

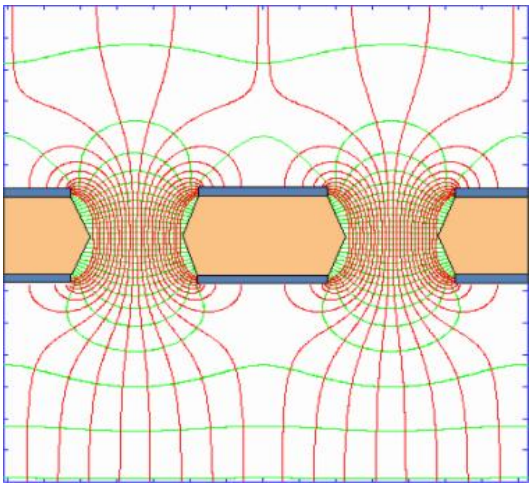

Figure 2.3: GEM foil field lines [21].

2.4 Two-Dimensional Readout

One of the nice advantages of the GEM neutron detector is the ability to design the readout structure according to the specifications of the application. Several different pickup plate designs are being considered for the current GEM detector, two of which will be discussed below. The first is a dog bone anode, which is seen in Fig. 2.4. It is a printed circuit board with orthogonal arrays of X and Y wires, which are woven from side to side of the board. The pitch of the lines is about 0.1 cm and the width of the lines is 0.015 cm. The electron

cloud amplified by the GEM foils is expected to overlap several of the X and Y signal lines resulting in a similar deposition of charge on each [22]. The individual lines are connected to surface mount resistor arrays that are on the sides of the board. The position of the electron cloud can be calculated by using the charge division equation, which is given by:

$$x / L = V_B /(V_A + V_B), \tag{2.1}$$

where L is the length of the wire, x is the position of the signal, and V_A and V_B are the voltages from the corners of the board for either the X or Y wire arrays.

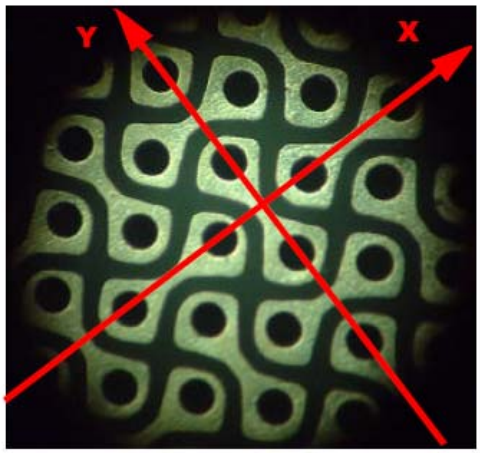

Figure 2.4: Close up of the dog bone anode, the x-y wire arrays are marked in red [22].

Another option for the readout structure is a two-dimensional position sensitive low distortion resistive anode [23]. The geometry of the resistive anode is shown in fig. 2.5.

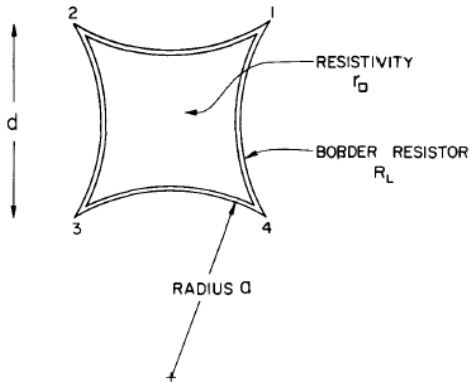

Figure 2.5: Resistive Anode pickup plate [23].

Four concave circular arcs of a given resistivity terminate the edges of the uniform resistive pickup plate [23]. It is then possible to calculate the position of the signal by:

$$x/d = \frac{I_1 + I_4}{I_1 + I_2 + I_3 + I_4}, \tag{2.2}$$

where x is the distance from the 1 and 4 vertices, d is length of the pickup plate, and I represents the currents measured at the 4 vertices of the pickup plate. A similar relation to calculate y, the position from the 3 and 4 vertices, can be also be derived.

Due to the fast drift of electrons in the field region before the anode, fast and short signals are induced on the anode, which leads to high rate capabilities.

Chapter 3 GEM Detector Monte Carlo Simulations

3.1 Overview of the Simulations

A number of simulations using the Monte Carlo electron/photon/positron transport code PENELOPE [24] have been performed in order to optimize and calculate several characteristics of the converter foil [25]. Integral and differential emission characteristics have both been calculated for various thicknesses of converter foils. These include the secondary electron yield, secondary electron escape probability, the pulse yield, and the average number of secondary electrons emitted from the converter foil when there is an emission. The secondary electron yield is defined as the average number of low energy electrons escaping the converter foil per incident particle. The pulse yield is defined as the probability that a secondary electron is emitted per incident particle. The 2001 version of PENELOPE was used in all simulations of the converter foil [24].

In order to make the following discussion clearer, the average number of low energy electrons generated per primary electron, will be denoted as δ and the average number of low energy electrons generated per incident neutron on the detector will be denoted as δ_n.

A similar denotation will be made for the pulse yields. The probability of producing a pulse per primary electron will be denoted as X, while the probability of producing a pulse per incident neutron will be given by X_p.

The definition of primary electrons is given to the conversation electrons emitted after neutron absorption. Secondary electrons are defined as those with energy less than 50 eV.

3.2 PENELOPE

PENELOPE simulates electron-photon showers in complex geometries produced by electrons, photons, or positrons. The operating energy range is between 100 eV and 1 GeV

and for materials involving elements with Z=1-92. Operation of the code is done by a simple steering program, which controls the core set of FORTRAN 77 subroutines.

Photon transport is treated by simulating all interactions during a photon history in chronological succession. Compton scattering, Rayleigh scattering, pair production, and photoelectric absorption are the considered interactions during photon transport [24]. All other interactions, such as photonuclear absorption, can be disregarded do to their smaller probability of occurrence [24].

During electron/positron transport, elastic scattering, inelastic scattering, radiative interactions, and positron annihilation events are all accounted for [24].

PENELOPE uses the so-called mixed simulation method to describe electron and positron transport [24]. In this method, cut off values are set for the energy loss and the angular deflection. Interactions are then categorized by these cutoffs into two groups. Hard interactions are simulated individually and have energy losses or angular deflections larger than the cutoffs. Soft interactions are those that involve small deflections and energy losses. A large number of these interactions occur between two hard interactions and therefore can be simulated as a single artificial event. The user can define simulation parameters in order to adjust the levels of the mixed simulation. Appendix A contains a sample PENELOPE input file and a description of the various parameters when running simulations for the double sided converter foil as discussed in the following sections.

PENELOPE also calculates the resulting depth-dose distribution in the CsI layers, defined as the average energy deposited per unit depth per primary electron. This is important in the calculation of the average number of secondary electrons emitted from the CsI, as discussed below.

3.3 Secondary Electron Emission Model

The process of electron induced secondary electron emission is a rather complex problem. The process can be divided into two general categories:

1) The slowing down of the primary electrons and the generation of secondary electrons

2) The created secondary electrons are then transported to the surface and escape

Incident electrons undergo elastic and inelastic interactions in the material which results in energy transfer to atomic electrons. A large cloud of secondary electrons begins to develop as these interactions occur repeatedly for newly generated secondary electrons. Once the energy of the electrons is below that of the band gap of the material, they interact with the lattice phonons, which result in small energy losses, and the transport of electrons resembles diffusion [26].

A series of papers by Akkerman and coworkers have addressed issues with secondary electron emission in alkali halides [27]. They have calculated secondary electron yields for CsI as a function of layer thickness. Their model "is based on the microscopic formulation of all electron interactions in the solid" [17]. Using Monte Carlo methods combined with their model, they follow electron transport within the CsI layer. Their model is free of semi empirical formulae and takes a first principles approach.

Optimization of the detector converter foil depends on the yields of the number of low energy secondary electrons emitted from its surface. However, due to the fact that PENELOPE can only calculate electron transport down to 100 eV, a semi empirical formula must be introduced in order to account for the low energy secondary electrons. The model involves two parameters: the energy to create a secondary electron Ω, and the escape depth

λ. The following formula can then be used to calculate the number of low energy secondary electrons emitted from the surface:

$$\delta = \int_{o}^{T} \frac{D(x)}{\Omega} \exp\left(\frac{-(T-x)}{\lambda}\right) dx \tag{3.1}$$

where T is the total thickness of the slab, D(x) is the depth dose distribution computed by PENELOPE, and x is a position within the slab. This model has then been fitted to data provided by Akkerman and co-workers.

Simulation results provided by Akkermam were reported for 3 keV energy electron beams incident on CsI slabs of various thicknesses. The model described above has then been fitted to these results (Fig. 3.1).

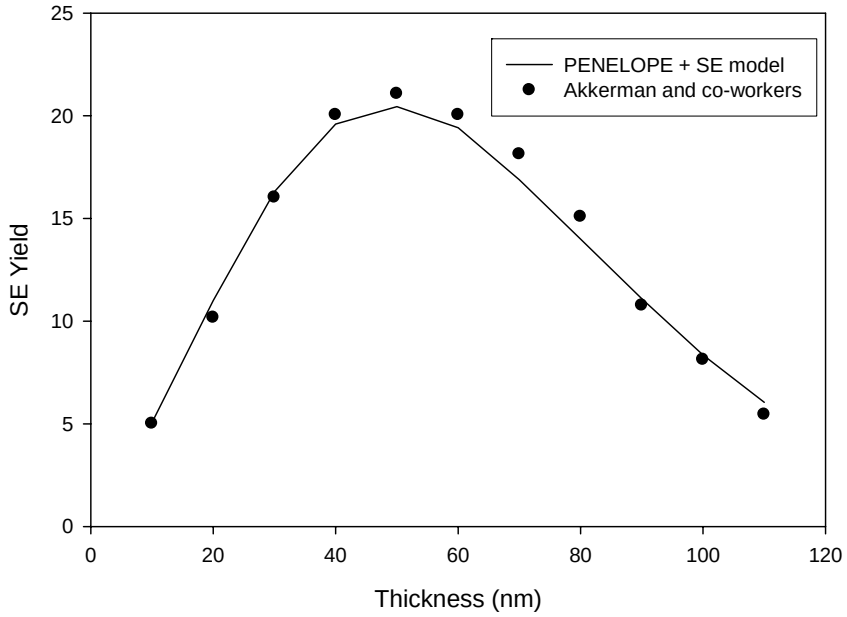

Figure 3.1: SE Yield fit to Akkerman data[27] with λ = 163 A and Ω = 15.2 eV

The optimum parameters were found by first doing a brute force grid search over the two-dimensional parameter space (Fig. 3.2). The brute force method first involved dividing the permissible range for each parameter into equal discrete units. The total parameter space

was then divided into cubes in which the value of S (the sum of the squared deviations weighted by respective errors) was calculated at each vertex and given by:

$$S = \sum \left[\frac{\delta_i - \delta(x_i)}{\sigma_i} \right]^2 \tag{3.2}$$

where δ_i is the secondary electron yield at x_i given by Akkerman, σ_i is the respective uncertainty for a given value of δ_i, and $\delta(x_i)$ is the value of the secondary electron yield calculated by PENELOPE and the semi-empirical model. The optimum parameters were found to be approximately $\lambda = 163$ A and $\Omega = 15.2$ eV.

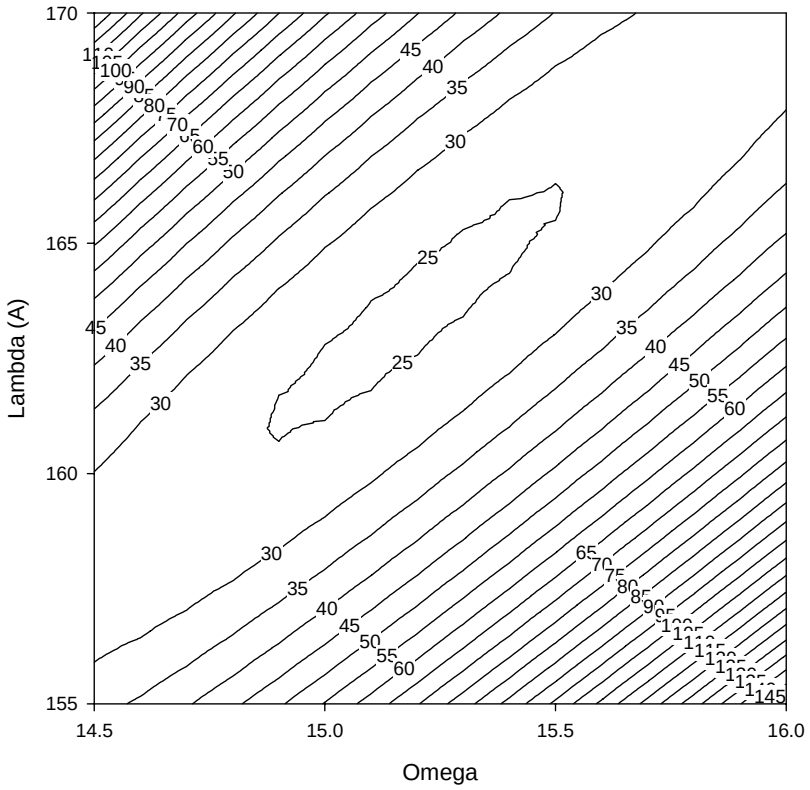

Figure 3.2: S as a function of lambda and omega.

3.4 Optimization of the Converter Sandwich

The subroutine PENCYL, contained in the PENELOPE package, was modified in order to simulate the performance of the converter foil. The material model employed is a

multilayered cylinder structure, in which each material of the converter foil is one of the layers in the cylinder. The cylinder is perpendicular to the direction of travel of the neutrons and is symmetric under rotations about its axis. In order to account for the absorption of the neutrons, the program samples the position of the primary electrons exponentially within the Gd layers. The emitted electrons have an energy sampled from the Gd conversion electron spectrum and their direction is isotropic.

3.4.1 Monte Carlo Random Sampling

A beam of neutrons that is incident on a material is attenuated and the fraction of the flux that passes through the layer can be described by the familiar exponential model given by:

$$I(x) = \frac{I}{I_0} = \exp[-(\Sigma_a \cdot x)] \tag{3.3}$$

where Σ_a is the macroscopic absorption cross section given in table 1.2 and x is the thickness of the Gd layer, I_0 is the intensity of the neutrons incident on the layer, and I is the intensity of the uncollided neutrons. In order to account for the neutron attenuation in a PENELOPE run, the position of the primary electrons needs to be weighted according to equation (3.3). This is done by sampling from the inverse of the cumulative distribution function.

The normalized probability distribution function from which the position of the electrons will be sampled from is given by:

$$A\int_0^\infty I(x)dx = 1 \tag{3.4}$$

in which A is the normalization constant so that the area underneath the curve is equal to 1. The probability distribution function is then:

$$f(x) = \Sigma_a \exp[-(\Sigma_a \cdot x)], \qquad x \le 0 \tag{3.5}$$

The cumulative distribution function used to describe (3.5) is the integral over **R** and is given by:

$$F(t) = \int_0^t \Sigma_a \exp[-(\Sigma_a \cdot x)]dx = 1 - \exp[-(\Sigma_a \cdot t)] \tag{3.6}$$

Sampling from the inverse of this distribution, when given a random number ξ, the value for t can be found by:

$$t = \frac{-\ln(1-\xi)}{\Sigma_a} \tag{3.7}$$

Since the number ξ is generated uniformly from 0 to 1, then equation (3.7) becomes:

$$t = \frac{-\ln(\xi)}{\Sigma_a} \tag{3.8}$$

Fig. 3.3 shows the distribution sampled from PENELOPE during one run. Equation (3.3) is plotted on the figure for comparison.

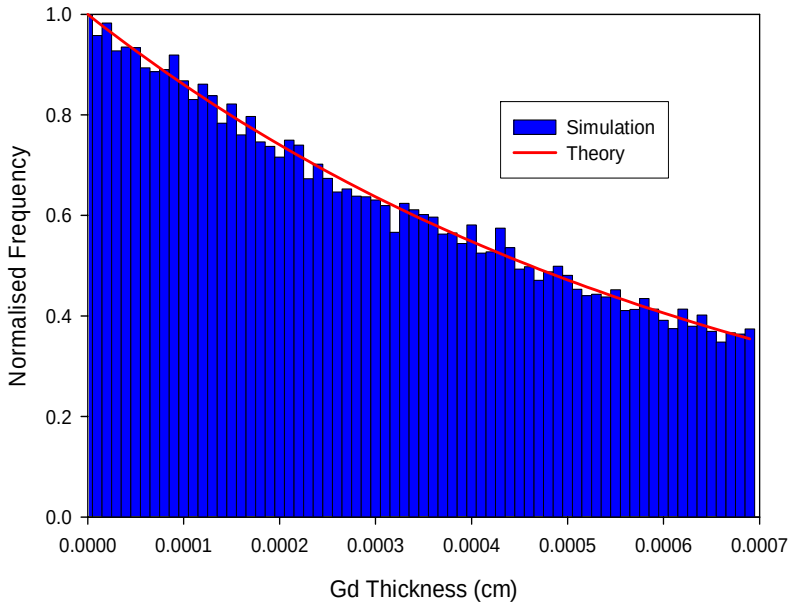

Figure 3.3: The simulated exponential distribution. The theoretical distribution, given by equation (3.2) is also on the plot.

3.4.2 Application of the Secondary Electron Emission Model

The secondary electron model and the exponential distribution discussed above were applied to the double-sided converter sandwich of various total Gd thicknesses. The secondary electron yield as a function of the Gd and CsI layer thickness is shown in Fig. 3.4. The Gd thickness in the figure represents the total thickness of the Gd used in the converter while the CsI thickness is that of a single layer of CsI on one side of the converter foil. A peak in the yield is seen around 0.1 micrometers while the yield increases as the Gd thickness is decreased.

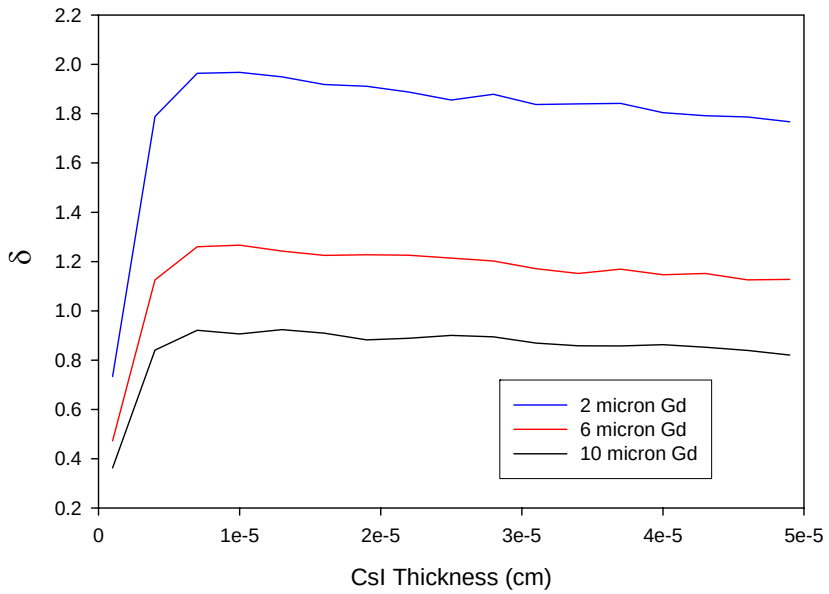

Figure 3.4: The secondary electron model applied to the converter foil.

In order to find the optimal layer thickness the results in Fig. 3.4 need to be weighted with the neutron absorption across the thickness of the Gd layers. The fraction of neutrons absorbed in a layer of Gd is given by:

$$1 - \exp[-(\Sigma_a \cdot x)] \tag{3.9}$$

where Σ_a is the macroscopic absorption cross section given in table 1.2 and x is the total thickness of the Gd layers.

A plot of equation (3.9) is shown in Fig. 3.5.

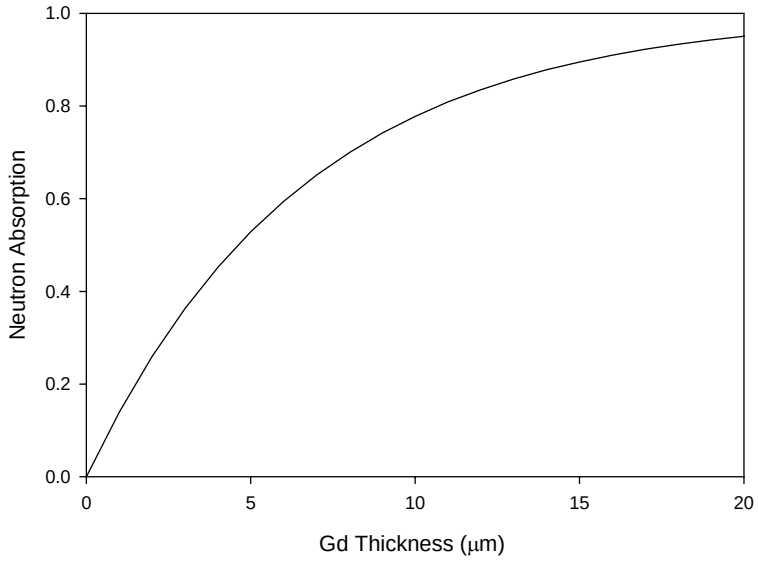

Figure 3.5: Gd Neutron absorption as a function of layer thickness

The average number of secondary electrons generated from the surface of the converter per incident neutron on the converter (δ_n) can be calculated by taking δ, the average number of secondary electrons emitted per primary (conversion) electron (the results in Fig. 3.4), weighted by the number of neutrons absorbed in a Gd layer, and the 86.5% efficiency of generating a primary electron per absorbed neutron and is given by:

$$\delta_n = \delta \cdot 0.865 \cdot \left[1 - \exp[-(\Sigma_a \cdot x)]\right] \tag{3.10}$$

This calculation was performed for both sides of the converter foil and the results were added together to get a total average number of secondary electrons generated per incident neutron from both sides of the converter foil. The results of this calculation are shown in Fig. 3.6. δ_n is presented as a function of the total thickness of the Gd and the single thickness of a CsI layer on one side of the converter foil. A broad maximum is seen in the secondary electron yield near 7 μm of Gd and around 0.1 μm of CsI. The average uncertainty in the yields is 5%.

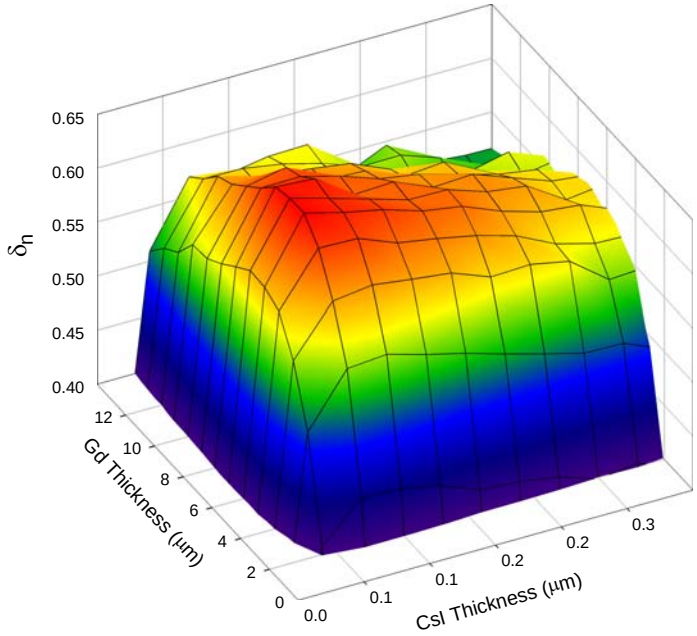

Figure 3.6: Weighted yields as a function of Gd and CsI thickness.

In order to address the dependence of the optimum thickness in Fig. 3.6 with the parameters chosen in Fig. 3.1, the values of λ and Ω were varied 15% in both directions. The results of these simulations are shown in Figs. 3.7 and 3.8. The optimum thickness of the converter foil is still consistent even with a change of 15% in the value of the parameters.

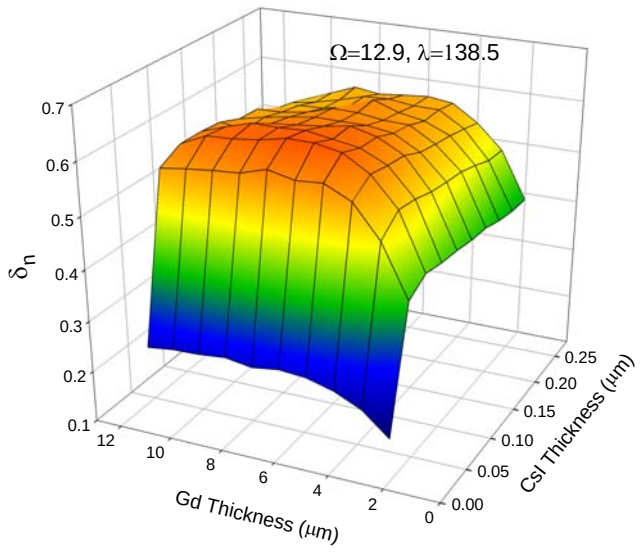

Figure 3.7: Converter foil with λ = 138.5 A and Ω = 12.9 eV.

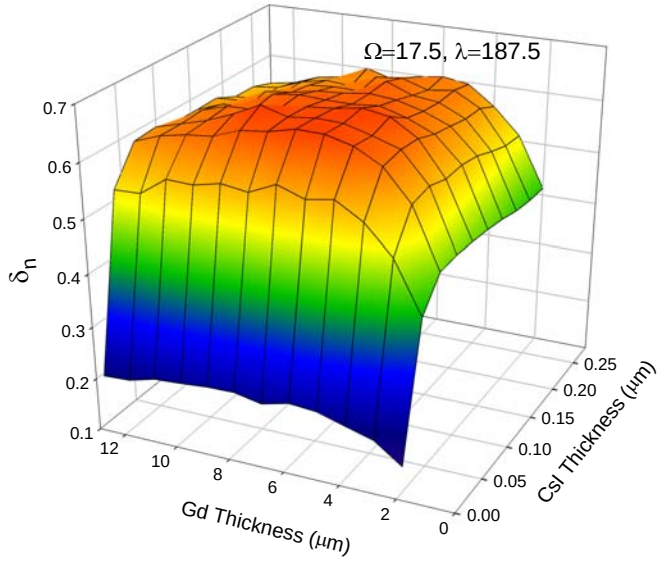

Figure 3.8: Converter foil with λ = 187.5 A and Ω = 17.5 eV.

The placement of the kapton foil within the entire thickness of 7 μm of Gd was also investigated. The CsI was set to 0.1 μm thick. Fig. 3.9 shows the effect of moving the kapton throughout the layer thickness. There is a maximum of 5% difference between moving the kapton from the center of the foil to the edges.

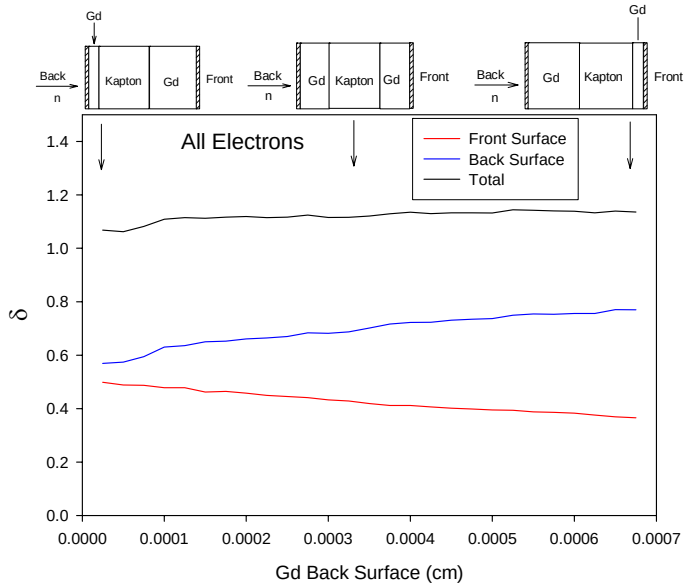

Figure 3.9: Placement of the kapton within the 7 μm thickness with 0.1μm CsI.

The effect of changing the thickness of the kapton is shown in table 3.1. While δ shows an increasing trend with decreasing kapton thickness, 7.5 μm foils have been used in detector construction for mechanical reasons. It becomes increasingly difficult to stretch thinner and thinner foils.

Table 3.1: The effect on δ when the kapton foil thickness varies for a converter with 7 μm thick Gd and 0.1 μm thick CsI.

Kapton foil thickness (μm)	δ
1.5	1.26
21.5	1.05
61.5	0.99
91.5	0.96

3.5 Multiple Module Detector

As shown in Fig. 3.4, the secondary electron yield increases as the thickness of the Gd layer decreases. It is possible to envision a detector that consists of multiple modules taking advantage of this increase in secondary electron yield while maintaining high neutron absorption efficiency.

There are two possible situations that can be realized when designing the detector. Each module could contain a converter foil with the same thickness of Gd. Another option is to design the detector so that the secondary electron yield from each module would be the same. In order to achieve this, the thickness of the Gd in each foil would be varied from one module to the next.

In all results given below, the CsI layers are 0.1 μm thick.

3.5.1 Multiple Modules, Equal Gd Thickness

Optimization of the detector based on multiple modules of the same Gd thickness requires that δ_n be calculated for each of the various detector setups. The total number of secondary

electrons produced in the detector is a sum of the number of secondary electrons produced in each module and is given by:

$$SE = \sum_{l=1}^{N} SE_l \tag{3.11}$$

where SE is the total number of secondary electrons in the detector, SE_l is the number of secondary electrons produced in a single module, l is respective module, and N is the total number of modules. Multiplying and dividing the number of secondary electrons in each module by the number of neutrons n_l, which is incident on the respective module, equation (3.11) becomes:

$$SE = \sum_{l=1}^{N} \frac{SE_l}{n_l} \cdot n_l \tag{3.12}$$

Since each of the converters contains the same thickness of Gd, equation (3.12) can be rewritten as:

$$SE = \left(\frac{SE}{n}\right)_x \sum_{l=1}^{N} n_l \tag{3.13}$$

where $\left(\frac{SE}{n}\right)_x$ is the value of δ_n for a single module detector of a thickness x as shown in Fig. 3.6. The number of neutrons incident on each module can then be written as a function of the number of neutrons incident on the first module.

$$n_l = n_1 \cdot e^{-\Sigma_a (l-1)x} \tag{3.14}$$

Substituting equation (3.14) into equation (3.13):

$$SE = \left(\frac{SE}{n}\right)_x \cdot \sum_{l=1}^{N} n_1 \cdot e^{-\Sigma_a (l-1)x} \tag{3.15}$$

Dividing by the number of neutrons incident on the first module, equation (3.15) becomes:

$$\delta_n = \frac{SE}{n_1} = \left(\frac{SE}{n}\right)_x \cdot \sum_{l=1}^{N} e^{-\Sigma_a (l-1)x} \tag{3.16}$$

The results of equation (3.16) are presented in Fig. 3.10. Saturation is reached for thicker Gd layers at a lower number of modules. Building a detector containing many thin layer converters would be the optimum detector. However, the number of modules employed will depend on the cost and the complexity of the decoding electronics.

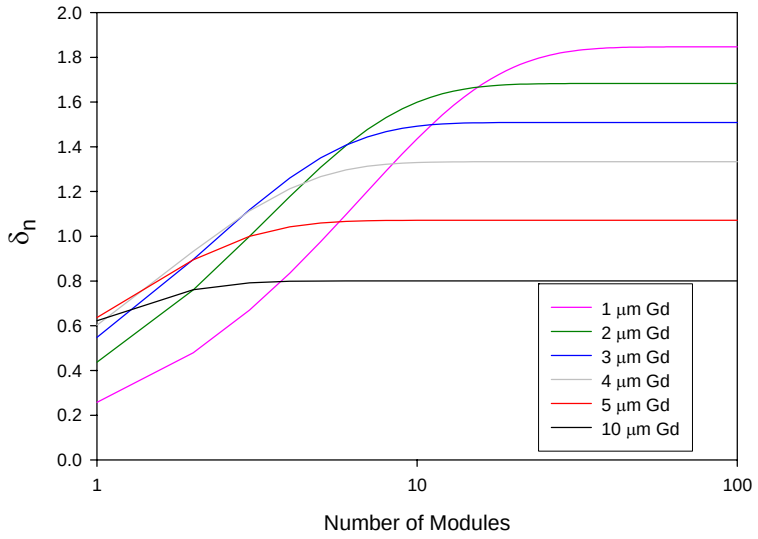

Figure 3. 10: δ_n as a function of the number of modules with λ = 163 A and Ω = 15.2 eV.

Table 3.2 illustrates the gain in δ_n for several different detectors in which 60% of the incident neutrons are absorbed. A gain of almost a factor of two is observed when going from one module of 6 μm of Gd to 6 modules each of 1 μm Gd. Tables 3.3 and 3.4 show the effect on the optimization by varying the parameters λ and Ω by 15%.

Table 3.2: Comparison of several detectors with 60% neutron absorption with λ = 163 A and Ω = 15.2 eV.

Gd Thickness (μm)	Number of Modules	Neutron Absorption	δ_n
1	6	60%	1.10
2	3	60%	1.01
3	2	60%	0.90
6	1	60%	0.64

Table 3.3: Comparison of several detectors with 60% neutron absorption with λ = 187.5 A and Ω = 17.5 eV.

Gd Thickness (μm)	Number of Modules	Neutron Absorption	δ_n
2	3	60%	0.97
3	2	60%	0.87
6	1	60%	0.62

Table 3.4: Comparison of several detectors with 60% neutron absorption with λ = 138.5 A and Ω = 12.9 eV.

Gd Thickness (μm)	Number of Modules	Neutron Absorption	δ_n
2	3	60%	1.02
3	2	60%	0.92
6	1	60%	0.65

3.5.2 Multiple Modules, Different Gd Thickness

An alternative detector design constraint is to require that each of the modules yield the same number of secondary electrons per neutron. The number of modules allowed in the detector is then dependent on the thickness of the converter foil in the first module. This constraint is given by the following equation:

$$\left(\frac{SE}{n}\right)_1 = \left(\frac{SE}{n}\right)_2 e^{(-\Sigma_a t_1)} = \left(\frac{SE}{n}\right)_3 e^{(-\Sigma_a (t_1+t_2))} = ... = \left(\frac{SE}{n}\right)_N e^{(-\Sigma_a (\sum_{l=1}^{N-1} t_l))} \tag{3.17}$$

where t_l is the thickness of the l^{th} layer.

Table 3.5 shows the results of imposing this constraint and calculating the number of modules, neutron absorption efficiency, δ_n, and the total Gd thickness used in the converter foil. A comparison with the results in table 3.2 shows that the maximum δ_n can be nearly achieved with a significant reduction in the number of modules if the thickness of the Gd is varied. The number and the complexity of the decoding electronics can be decreased by building a detector with multiple modules in which the thickness of each module is allowed to be different.

Table 3.5: Detector with multiple different Gd thickness modules and λ = 163 A and Ω = 15.2 eV.

First layer Gd Thickness	Total Gd Thickness (μm)	Number of Modules	Neutron Absorption Efficiency	δ_n
0.1	29	98	99%	1.17
0.2	21.5	40	96%	1.58
0.4	16	16	91%	1.68
0.6	11	9	81%	1.52
0.8	8.9	6	74%	1.36
1	6	4	60%	1.10

3.6 Electron Escape Probability Histograms and Pulse Yields

As a further test of the secondary electron model discussed above, the pulse yields for various Gd-CsI converters were also calculated. The pulse yield is defined as the probability that any number of secondary electrons is emitted from the surface of the converter per incident particle. The pulse yield represents the converters ability to convert the incident neutron to a detectable electric signal, and is therefore directly related to the detection efficiency of the detector.

Calculation of the pulse yield first requires simulation of the electron escape probability distribution. The electron escape probability distribution is defined as the probability that any number of secondary electrons is emitted from the surface of the converter foil per incident particle. Akkerman and co-workers have calculated electron escape histograms for various energies of x-rays (per one absorbed photon) with normal incidence to CsI photocathodes of various thicknesses [28]. Under the assumption that the escape mechanism of the secondary electrons in CsI is the same for electron and photon induced emission, the model discussed above has been applied to the case in which photons are incident on a CsI layer. Results from the simulations (per one absorbed photon) are compared with those of Akkerman and co-workers for 60 keV photons incident on a 4.5 μm layer of CsI as shown in Fig. 3.11.

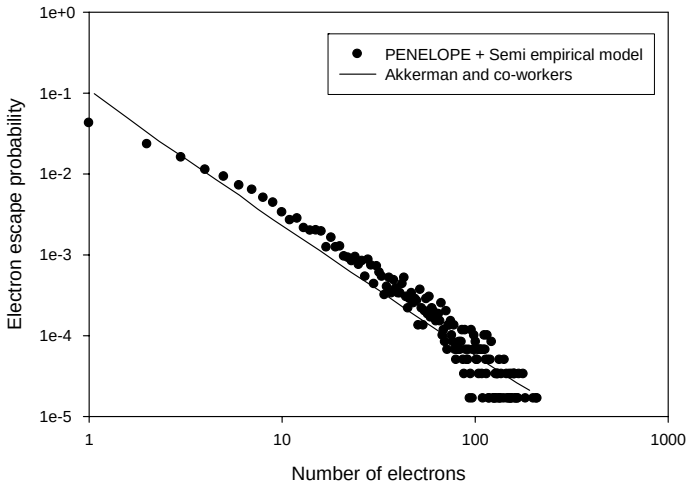

Figure 3.11: Electron escape probability distribution (per one absorbed photon) for 60 keV photons with normal incidence to a 4.5 μm slab of CsI compared with data from [28].

The pulse yield can then be calculated by integrating the distribution in Fig. 3.11 and by taking into account the probability of x-ray absorption in the layer. The calculated values for the pulse yields are compared to Akkerman's data for several different thicknesses for 60 keV photons incident on the CsI layer as shown in Fig. 3.12.

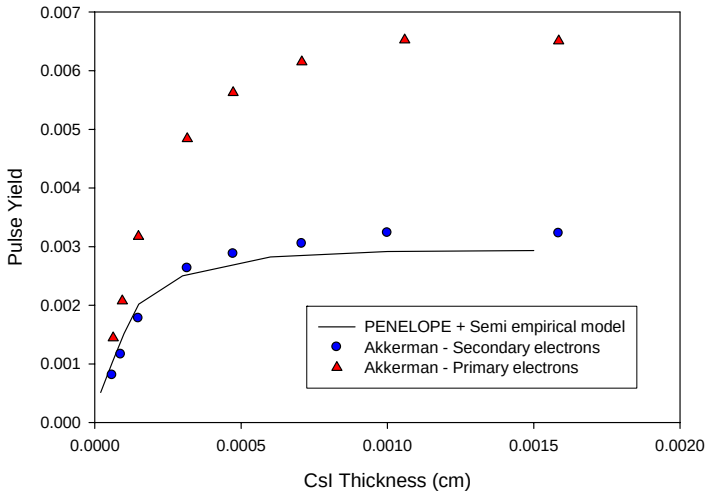

Figure 3.12: Pulse yields (per incident photon) for 60 keV photons with normal incident to the CsI layers compared with [28].

The results shown in Fig. 3.12 have the same trends as Akkerman's data. There is saturation in the pulse yield as the thickness increases. However, the pulse yields calculated

by the combined PENELOPE and semi-empirical model are slightly less at greater thicknesses than those calculated by Akkerman and co-workers.

3.7 Simulation of the Detector Pulse Yield

Similar electron statistics and pulse yields have been calculated for the CsI-Gd-kapton converter foil sandwich. In order to make discussion easier, it is important to define the relationship between the pulse yield X and δ. The secondary electron yield δ is a quantity averaged over the total number of conversation electrons simulated, and can be represented by the following equation:

$$\delta = \frac{\sum_{i=1}^{N} SE_i}{N} \tag{3.18}$$

where N is the total number of histories, and SE_i is the number of secondary electrons released from the converter foil for the i^{th} history. By placing the number of secondary electrons created (at least 1 secondary electron) in the i^{th} history into a respective bin, the following formula represents the pulse yield:

$$X = \frac{\sum_{j=1}^{J} SE_j}{N} \tag{3.19}$$

where SE_j is the frequency in the respective bin j, J is the total number of bins, and N is the total number of histories. The relationship between these two quantities is $\bar{n}$, the average number of electrons emitted in a pulse and is given by:

$$\bar{n} = \frac{\sum_{i=1}^{N} SE_i}{\sum_{j=1}^{J} SE_j} = \frac{\delta}{X} \tag{3.20}$$

From equation 3.19, optimization of δ can be interpreted as the optimization of the product of the pulse yield times the average number of electrons emitted in a pulse. The same equation holds true for these quantities when they are normalized per incident neutron, i.e. δ_p and X_p.

The electron escape probability histograms for the optimum case of a single module with 7.5 μm of kapton, 0.1 μm CsI, and 7 μm total of Gd is shown in Fig. 3.13. Both the distributions for the forward and back secondary electron emission is shown. Forward emission is defined as the emission from the downstream (relative to the neutron beam) side of the converter, while backward emission is from the upstream side.

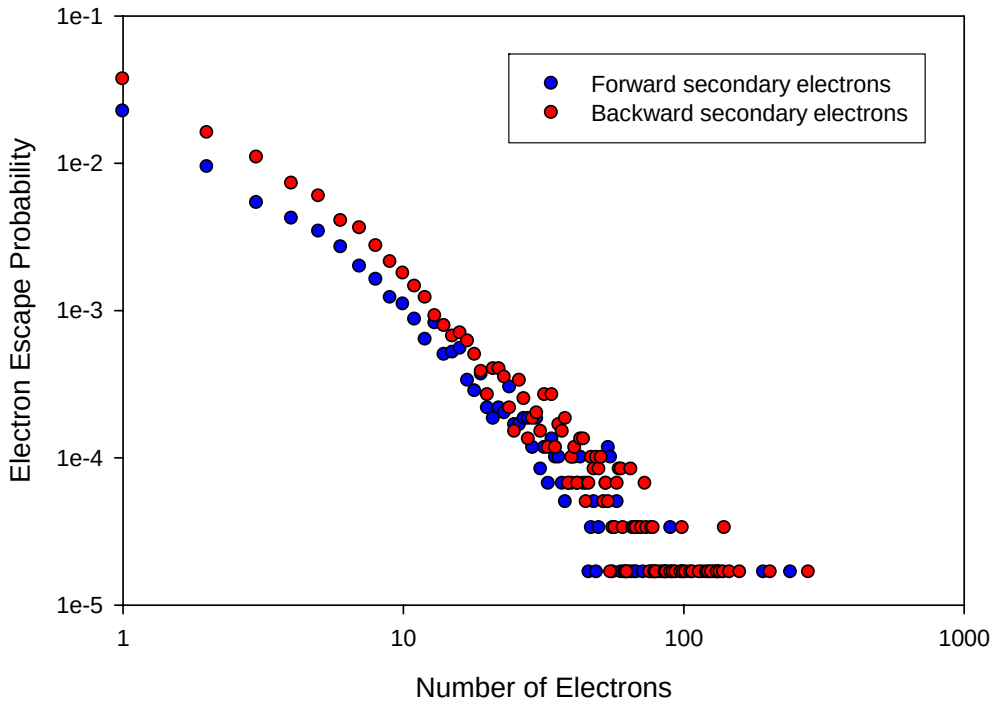

Figure 3.13: Electron escape probability histogram (per primary electron) for the optimized single converter foil.

The total electron escape probability distribution is shown in Fig. 3.14. The total probability distribution histogram represents the situation in which a certain number of electrons are released from the entire sandwich converter.

The pulse yield X_p is then calculated by integrating these distributions and by taking into the account the neutron absorption across the Gd layer. Using equation (3.20) and the values for δ_n from Fig. 3.6, the integral characteristics in table 3.6 can be deduced.

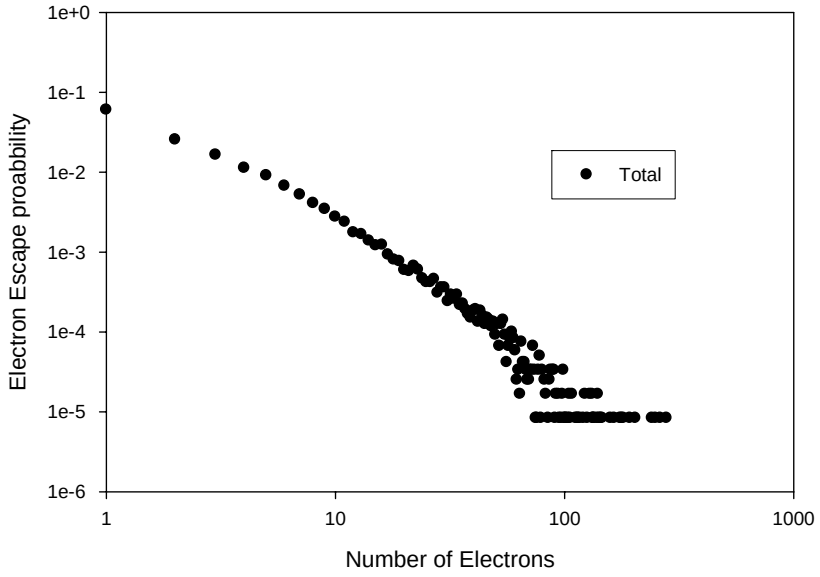

Figure 3.14: The total electron escape probability histogram for the optimized converter foil.

Table 3.6: Integral characteristics for the optimum converter foil in Fig. 3.14.

	Forward	Backward	Total
δ_n	0.25	0.42	0.67
X_n	0.036	0.06	0.096
$\bar{n}$	~7	~7	~7

The quantities listed in table 3.6 show important characteristics of the detector. The converter pulse yield of 0.096 would be the maximum possible efficiency of a single module GEM neutron detector. The average number of electrons released in a pulse is not very large. The CsI is sensitive to photons and will produce pulses, which are on the same order of

magnitude as those produced by the primary electrons. A pulse produced by an x-ray will be counted in the same manner as a pulse produced by a primary electron. This means that a method for discrimination against x-rays will be necessary.

Chapter 4 Detector Construction and Electronics

4.1 Overview of the Detector Components

The basic overview of the infrastructure of the detector is shown in Fig. 4.1. The detector functions with two power supplies, one to control the anode bias, one to control the cathode and GEM bias, and the common general purpose fill gas known as P-10 (90% argon, 10% methane).

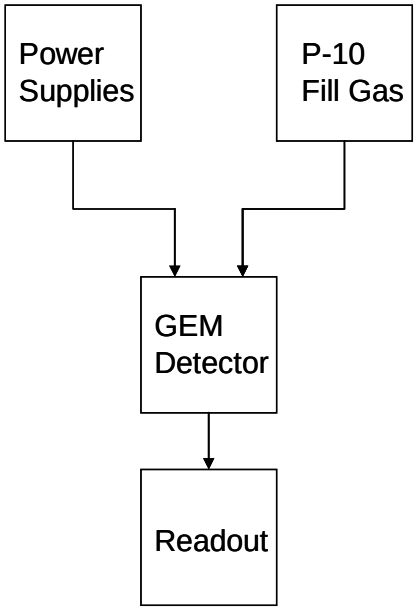

Figure 4.1: Overview of the detector setup.

Two different prototype detectors have been designed and built during the course of this work. The first detector (prototype 1) was built before the beginning of this project but was not extensively tested. The detector has a ^{nat}Gd converter with 5 μm ^{nat}Gd and 5 μm CsI evaporated on a 0.125 inch Al substrate. These dimensions for the converter foil were chosen before the completion of the PENELOPE simulations. The second detector (prototype 2) has been constructed throughout the course of this work and contains a boron converter instead of a Gd-CsI sandwich. This choice was made to better understand the position encoding and general characteristics of the GEM detector, which will be discussed below. Prototype 2

contains only the lower GEM foil. Otherwise, each detector prototype uses the same basic components and units as seen in Fig. 4.1.

Throughout the testing of prototype 1 and 2 detectors, it became apparent that the design of the detectors might equally function as a beam monitor for neutron scattering instruments. The purpose of a neutron beam monitor is to characterize beam attributes, such as intensity and spatial and time distributions at neutron scattering instruments. A beam monitor can be used during neutron scattering experiments to normalize the data collected from instruments. The detection efficiency of such a detector was discussed with several of the instrument scientists at the SNS and should be on the order of 10^{-5} to 10^{-7} [29]. Differences between prototype 1 and 2 will be discussed in further detail.

Fig. 4.2 shows the vertical structure of a half module for detector prototype 1 and Fig. 4.3 shows the vertical structure for prototype 2.

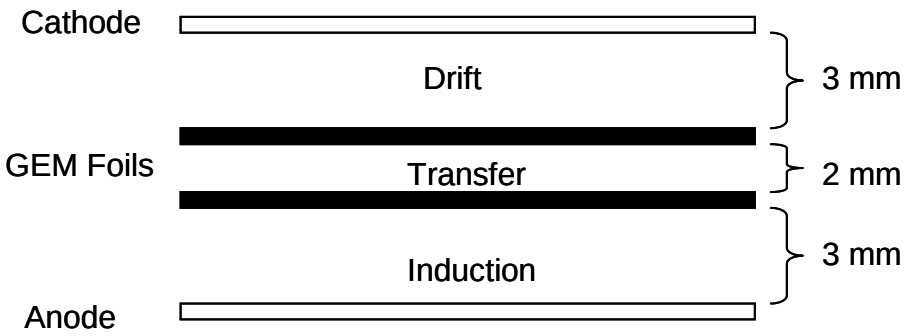

Figure 4.2: Vertical structure of a detector half module for prototype 1.

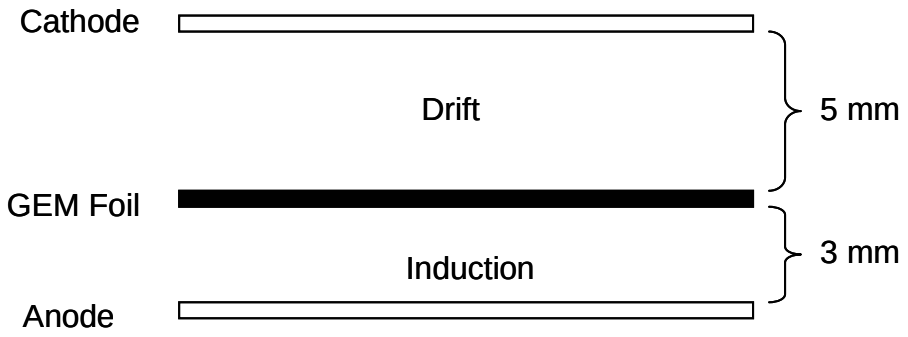

Figure 4.3: Vertical structure of a detector half module for prototype 2.

The components in Fig. 4.2 and 4.3 can easily be swapped or replaced. Each component of the detector is independent of each other. The number of GEM foils, type of cathode and anode, can all be easily changed when using this technology.

These characteristics show the versatility of the GEM detector technology. Two detectors, for different applications, were essentially constructed from the same components and electronics.

The interior of both prototype 1 and prototype 2 are shown in Figs. 4.4 and 4.5. The completed detectors are shown in Figs. 4.6 and 4.7.

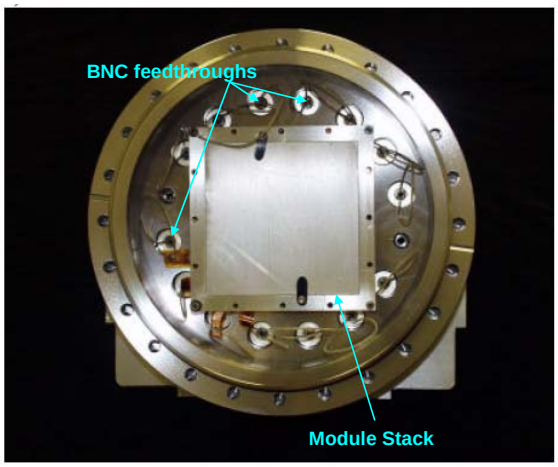

Figure 4.4: Prototype 1 Interior.

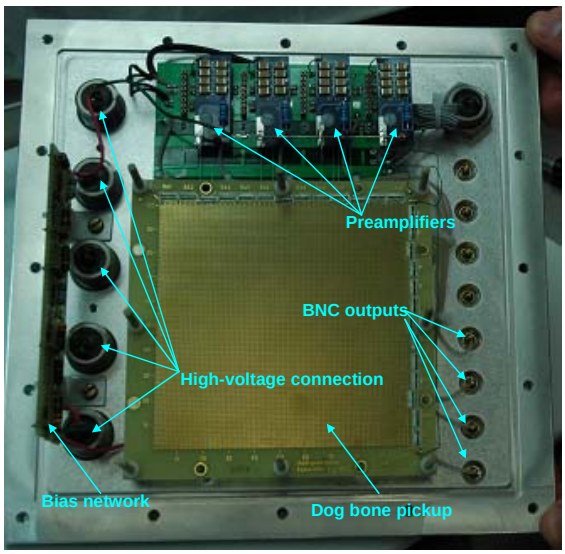

Figure 4.5: Prototype 2 Interior.

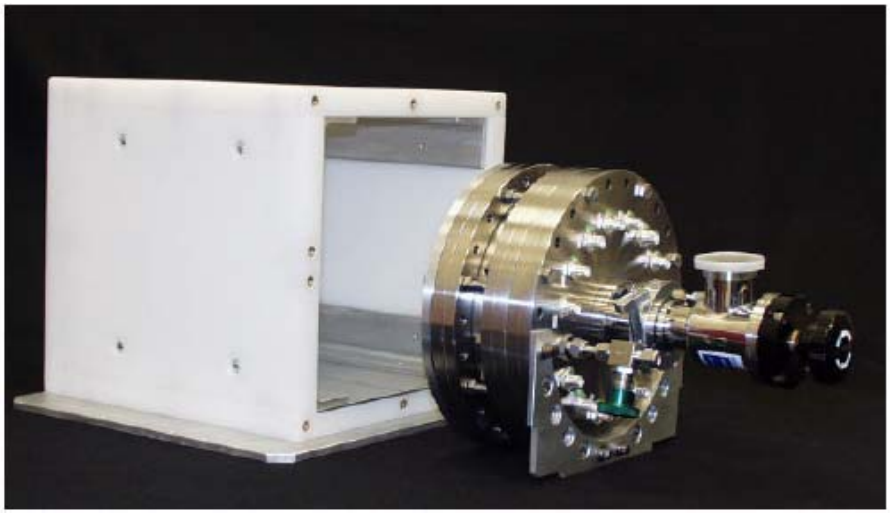

Figure 4.6: The completed prototype 1 detector with 1 inch thick borated poly shielding [22].

Figure 4.7: The completed prototype 2 detector in its housing.

The detector housing for prototype 1 is made of stainless steel and for prototype 2 it is made of aluminum. Both detectors have a 3 mm thick aluminum entrance window. For both prototypes the readout board along with the GEM foils and the cathode are mounted with polymer screws to the housing of the detector. In prototype 1 both the preamplifiers and the resistor bias board have been placed outside of the detector housing. This choice was made

early on in the project to allow flexibility for prototype 1. For prototype 2, the resistor bias board is connected to the high voltage vacuum feedthroughs and then connected to the various detector components. The preamplifiers have also been placed inside the detector housing, which should reduce electronic noise. Signals from the preamplifiers are sent through the BNC outputs to the position encoding electronics. The active area of the detector is 100 cm^2. Each detector is shielded by 1 inch thick borated poly.

4.2 Detector Fill Gas

Cheap neutron counting gas can be used in the GEM neutron detector due to the decoupling of the converter and the detection of the neutron signal. The detector is operated in continuous flow mode with the common counting gas P-10.

4.3.1 Detector Biasing and Electric Fields for Prototype 1

A resistor bias network has been created in order to apply the bias across each of the detector components. The detector can then be biased easily with only two high voltage power supplies. The biasing network is shown in Fig. 4.8. The 10 MΩ resistors, which are shown in Fig. 4.8, limit the current through the various units.

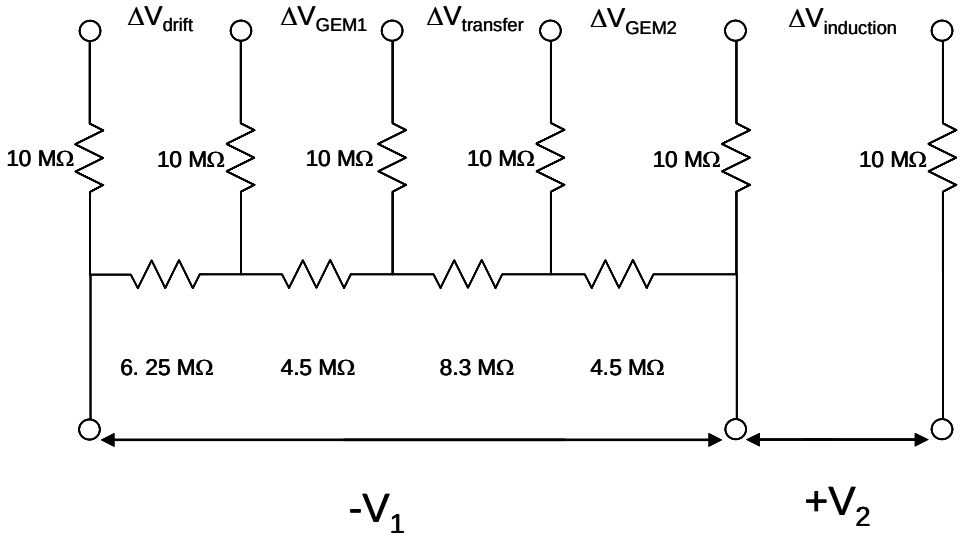

Figure 4.8: Detector Bias network

In prototype 1 there are three distinct regions where electrons are transferred, the drift region, where the ionization electrons are created and drifted towards the first GEM, the transfer region between the two GEMs, and the induction region where the electrons are collected at the anode. Table 4.1 summarizes the electric fields between each of the components in the GEM foil and the voltages placed across the GEMs when at operating voltage.

Table 4.1: Fields and voltages during operating conditions for prototype 1.

	Formula	At Operating Voltage
Cathode	V_1	1900 V
Anode	V_2	900 V
Drift Field	0.27 V_1 / 3 mm	1.71 kV/cm
Transfer Field	0.35 V_1 / 2 mm	3.33 kV/cm
Induction Field	V_2 / 3 mm	3.00 kV/cm
GEM 1 and 2 Voltage	0.19 V_1	361 V

Careful selection of the drift fields and GEM voltages are important when designing the detector. Because only a low number of secondary electrons are emitted from the surface of the converter, poor selection of the fields could result in the loss of several of those electrons. This could lead to a deterioration of the detector performance because there would be a possibility for the complete loss of an event. If the drift field is too strong, some electric field lines will terminate on the top electrode of the GEM, thereby allowing for only a fraction of the drifting electrons to be collected in the GEM holes. Optimum conditions for transfer across the GEM foils have been seen when the drift region has a lower electric field than the transfer region [30]. When operating two GEMs in series, the transfer field essentially acts as the drift field for the second GEM foil.

GEM gains as a function of voltage have been extensively studied and measured in various gas mixtures for different combinations of GEM foils in series. Fig. 4.9 shows charge gains measured by P.R.B Marinho etc al.for various gas mixtures [31]. The field designations used in the figure is the same as shown in Fig. 4.2.

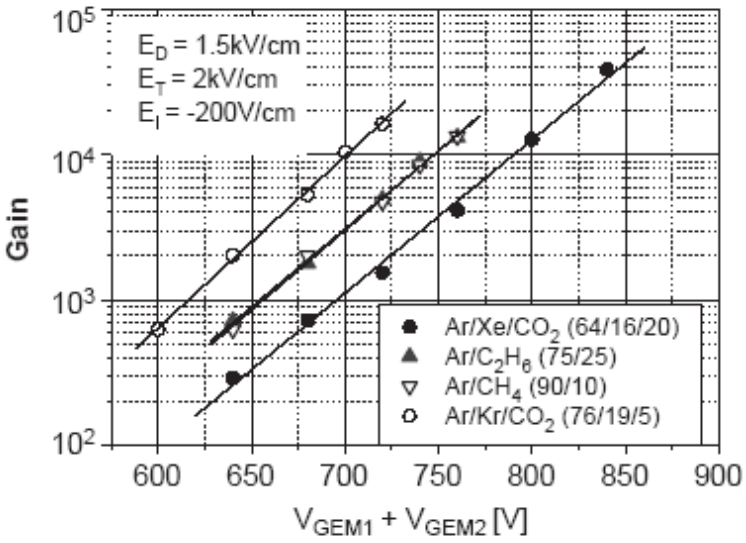

Figure 4.9: Charge gain has a function of the total voltage across the GEMs [31].

Fig. 4.9 shows that when operating the GEMs at 361 V in P-10 (Ar/CH_4 90/10) the charge gain is just above 3×10^3.

The signal to noise ratio in the detector can be increased by operating the GEM foils at a high bias. However, this leads to potential damage caused by sparks due to discharge. The usage of one or more GEM foils also allows for the reduction of the voltage across each GEM in the detector. This reduces the risk of severe discharges in the components, which can lead to permanent damage.

Significant tests of the effect of the GEM fields and voltages on the count rate were not completed due to experimental problems with detector prototype 1, which will be discussed in more detail in the next chapter.

4.3.2 Detector Biasing and Electric Fields for Prototype 2

The resistor bias network for detector prototype 2 is essentially the same as seen in Fig. 4.8. However, since the first GEM foil has been omitted, there is no transfer region in the detector. The induction distance for the drift gap is 5 mm and for the induction gap it is 3 mm. Table 4.2 shows the field and voltage settings for prototype 2.

Table 4.2: The field and voltage properties for prototype 2.

	Formula	At Operating Voltage
Cathode	V_1	2000 V
Anode	V_2	1100 V
Drift Field	0.81 V_1 / 5 mm	3.24 kV/cm
Induction Field	V_2 / 3 mm	3.66 kV/cm
GEM 1 Voltage	0.19 V_1	361 V

Due to the large ionization created by the reaction products in the ^{10}B capture reaction; the selection of the fields is not as important as discussed above for prototype 1. In a situation where there is a large number of electrons created by the ionization products, the transfer efficiency should only affect the resolution of the pulse height distribution [30].

The field strength for the induction field was chosen by holding the drift field strength at 3.24 kV/cm while varying the anode voltage. The counts per second as a function of anode voltage are shown in Fig. 4.10 for prototype 2 exposed to a 1.478 A beam of neutrons. Increasing the anode voltage above 600 V produces no significant difference in the count rate. The final choice of the electric fields was based solely on the effect that the fields had on the pulse height distribution resolution. This will be discussed in detail in the next chapter. A more detailed optimization of the fields in the detector could be completed in the future.

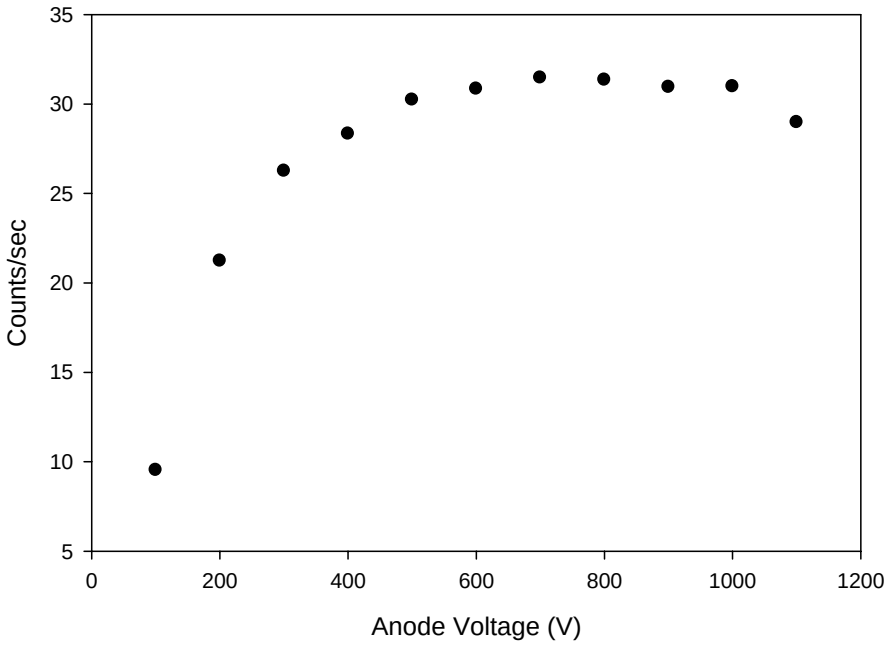

Figure 4.10: Counts/s versus anode voltage for prototype 2

4.4 Cathode Construction

The Gd and CsI evaporations for the converter foil in prototype 1 were completed by Douglas McGregor at the S.M.A.R.T laboratory of Kansas State University [32]. The thickness of the respective layers is 5 μm ^{nat}Gd and 5 μm CsI and they have been deposited on a 0.125 inch thick Al plate. These thicknesses were chosen before the completion of the PENELOPE simulations.

Two different methods for creating cathode screens using Boron were attempted. The first was using drops of ^{nat}B and Douglas McGregor at the S.M.A.R.T laboratory completed the second by evaporating ^{10}B.

The first attempt at creating boron cathode was completed by mixing ^{nat}B powder with water. A 1% ^{nat}B solution was created and drops were placed in a 5X5 array on a printed circuit board coated with copper. The thickness of the drops was estimated to be close to 4 μm thick with a diameter of 3 mm. The completed cathode screen is shown in Fig. 4.11.

Figure 4.11: ^{nat}B converter screen.

The second converter foil was created at Kansas State University by evaporating ^{10}B through a kapton stencil with 2 mm holes and 14 mm spacing. Fig. 4.12 shows the completed ^{10}B converter screen. The thickness of the dots is 1000 A.

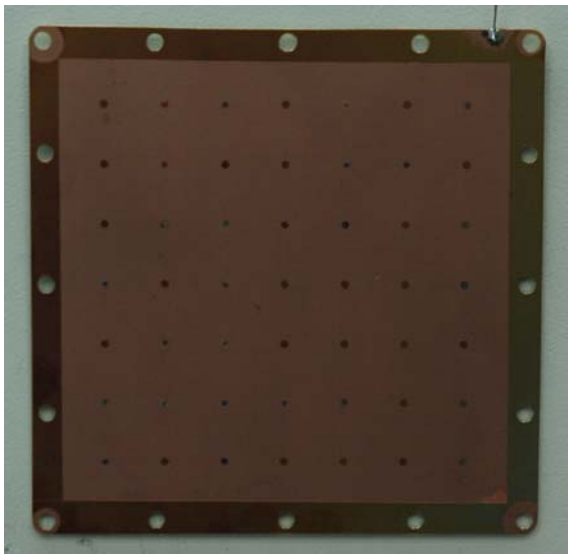

Figure 4.12: ^{10}B converter foil.

The theoretical efficiency of detectors that employ these cathode screens is shown in Fig. 4.13. A converter with 4 μm of ^{nat}B is just slightly greater than 1%. For a 1000 A ^{10}B converter screen the efficiency is close to 0.5%.

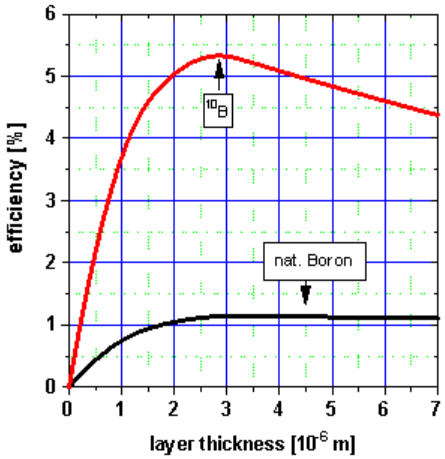

Figure 4.13: Efficiency of single B converters in the forward direction [33].

4.5 Kapton and GEM Foil Stretching

The stretching of the kapton converter foil and the GEM foils were accomplished in the same manner. The GEM foils were supplied by Tech-Etch [34] with 5 μm copper deposited on both sides of a 0.051 mm kapton foil. Fig. 4.14 shows the mounting apparatus designed and used in the stretching of the GEM foils and Fig. 4.15 shows a mounted GEM foil along with two frames.

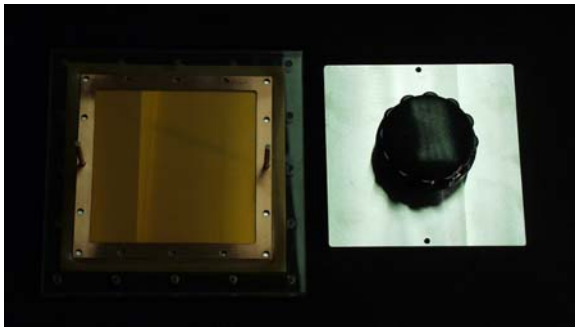

Figure 4.14: The mounting apparatus.

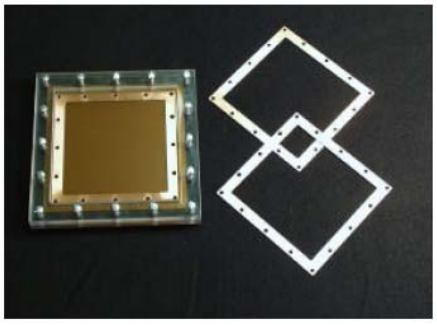

Figure 4.15: Mounted GEM foil and two mounting frames

The foils were first stretched and placed into plexiglass picture frames and were heated to 60 ^{o}C. After heating for 30-40 minutes the frames are removed from the oven and glued to printed circuit board frames on both sides with epoxy. The glued structure is then returned to the oven where the warm plexiglass uniformly stretches the foil. After the epoxy has cured, the structure is removed from the oven and the plexiglass stretching frame is removed

4.6 Detector Position Encoding

The position encoding schematic of the dog-bone readout board discussed in chapter 2 is shown in Fig. 4.16.

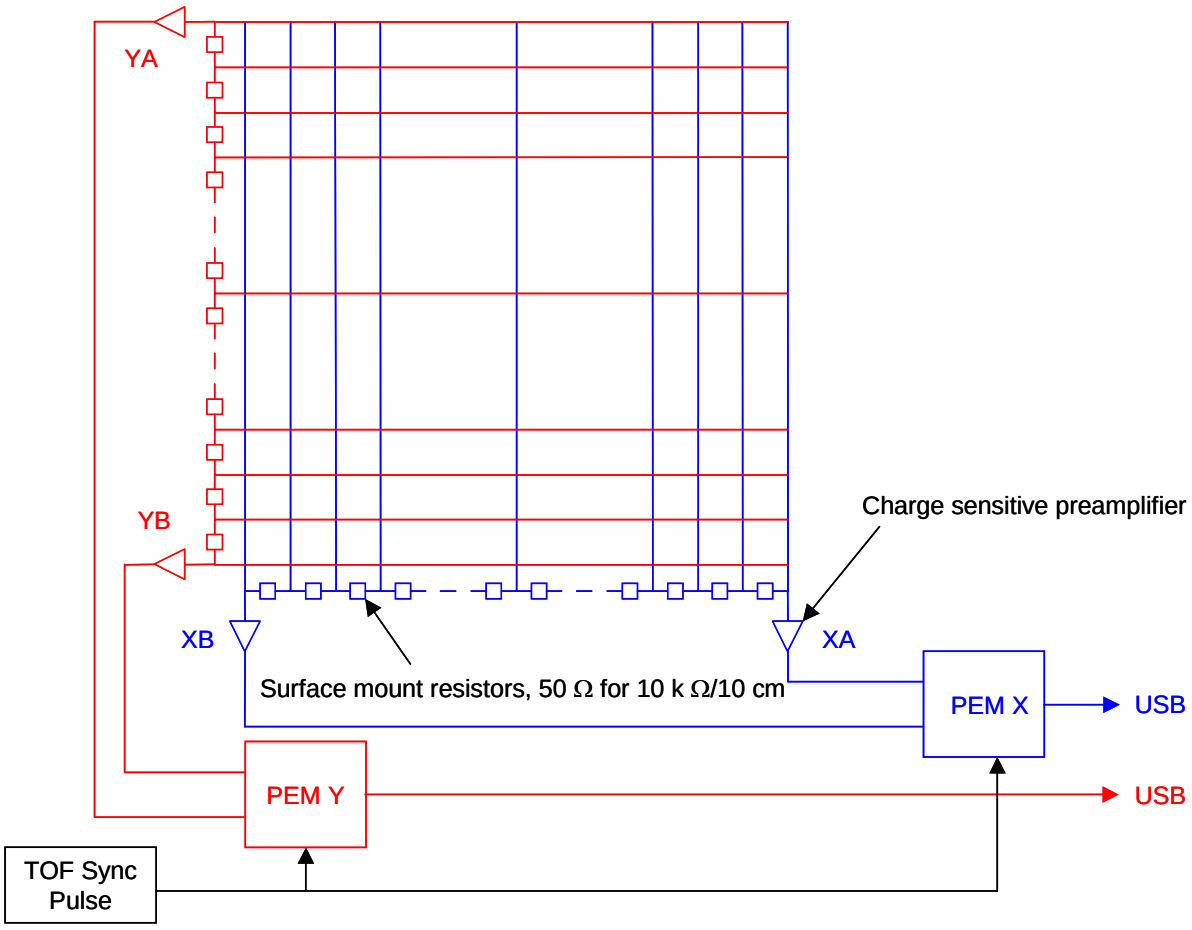

Figure 4.16: Position Decoding schematic.

The dog bone pickup is fabricated using printed circuit board (PCB). Each of the x-wires and each of the y-wires are connected via a series of 50 Ω surface mount resistors. Currents at the four corners are sent through charge sensitive preamplifiers and then to two Instrumentation Associates [35] position encoding modules (PEMs). The block diagram for a PEM half channel is seen in Fig. 4.17. One PEM is needed for XA, XB, and one for YA, YB.

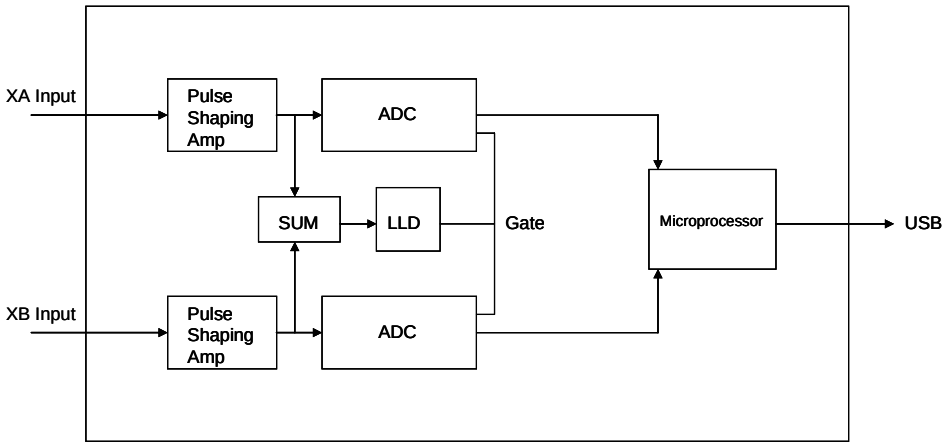

Figure 4.17: PEM half channel.

The PEMs are each 1-wide NIM enclosures, which are supplied with power from a NIM bin and NIM power supply. The module contains two linear pulse-shaping amplifiers, two 16-bit successive approximation ADCs, a summing amplifier, and an integral discriminator. The preamp signals are connected via BNC to the PEM module. Signals from the sum amplifier that exceed the LLD cause the signals at the XA and XB input to be digitized by the ADCs. The data are then sent local storage where they are periodically sent to the host computer via USB 2.0 protocol with a data transfer rate of 20 MByte/sec. Incoming data is then time stamped with reference to a TOF sync pulse. The host computer then sorts the x- and y-data by the TOF time stamp to correlate the events and reject events that contain only x- or y-events.

An extensive instrument control program, written in Java by Instrumentation Associates, was used to control the data acquisition of the detector. The program allows for

control of the gain, zeros, and LLDs of each of the PEMs. The program also downloads the XA, XB, YA, and Y-B amplitudes and produces respective histograms of the pulse height in each side, two-dimensional plots of the neutron intensity at the face of the detector, and the TOF histogram. Raw data and TOF filtered data are also plotted. The program also saves the data into a list format for later analysis.

4.7 Detector NIM Bin Modules

The entire detector electronic setup is shown in Fig. 4.18. The whole system requires two high-voltage power supplies, one for the cathode and one for the anode, two PEMs, one for both the x and y-sides of the readout board, a sync pulser and buffer, preamp power module, a test pulser, and a counter/timer. The test pulser serves as a means for testing the preamplifiers and calibrating the PEMs as discussed below.

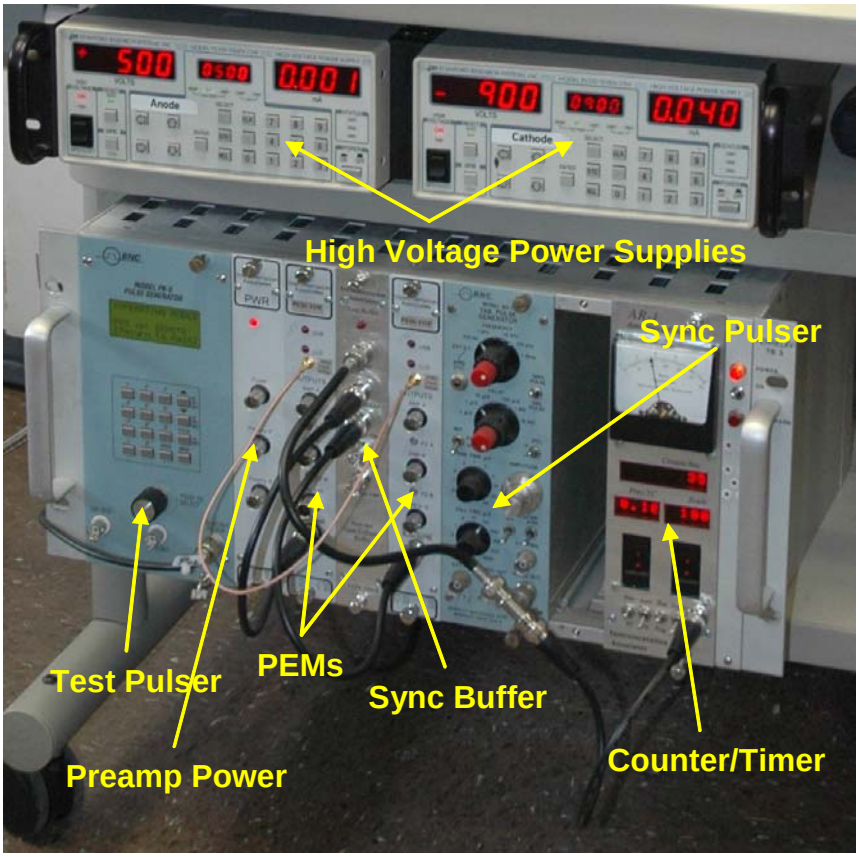

Figure 4.18: The electronic rack used during the detector experiments.

Typical preamplifier signals and neutron pulses taken with the detector prototype 2 are shown in Figs. 4.19 and 4.20. Both scope pictures were taken with a LeCroy oscilloscope [36].

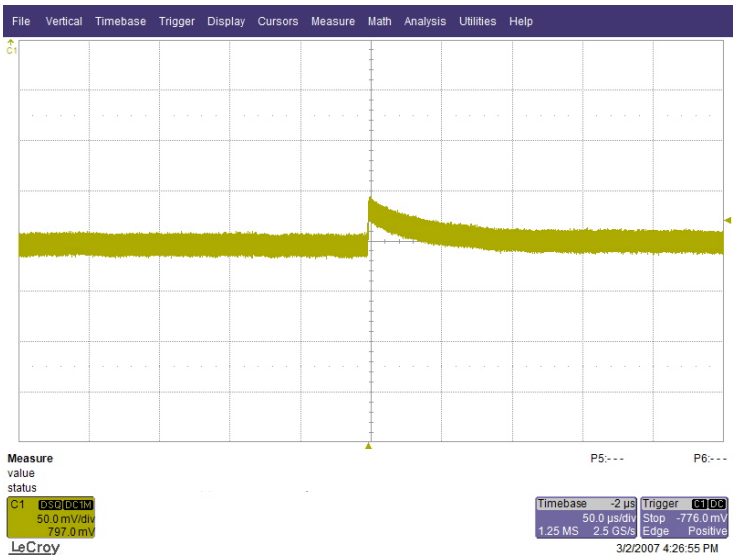

Figure 4.19: Preamplifier signal.

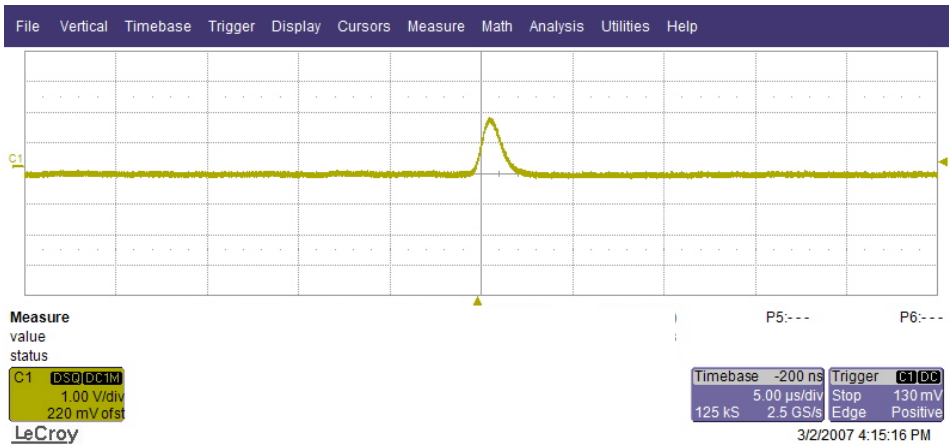

Figure 4.20: Typical neutron pulse.

4.8 Calibration of the PEMs

Calibration of the PEMs is similar to that of a multichannel analyzer (MCA). An ideal situation would be when the PEMs perform a perfect linear conversion of pulse height to channel number. The test pulser is used to provide peaks of known amplitude and provide points for a calibration plot. Fig. 4.21 shows plots of the pulse height spectra for the XA, XB,

YA, and YB outputs of the PEMs when using a test pulser for calibration. A measurement of the channel number versus pulser amplitude is shown in Fig. 4.22 for the XA output of one of the PEMs.

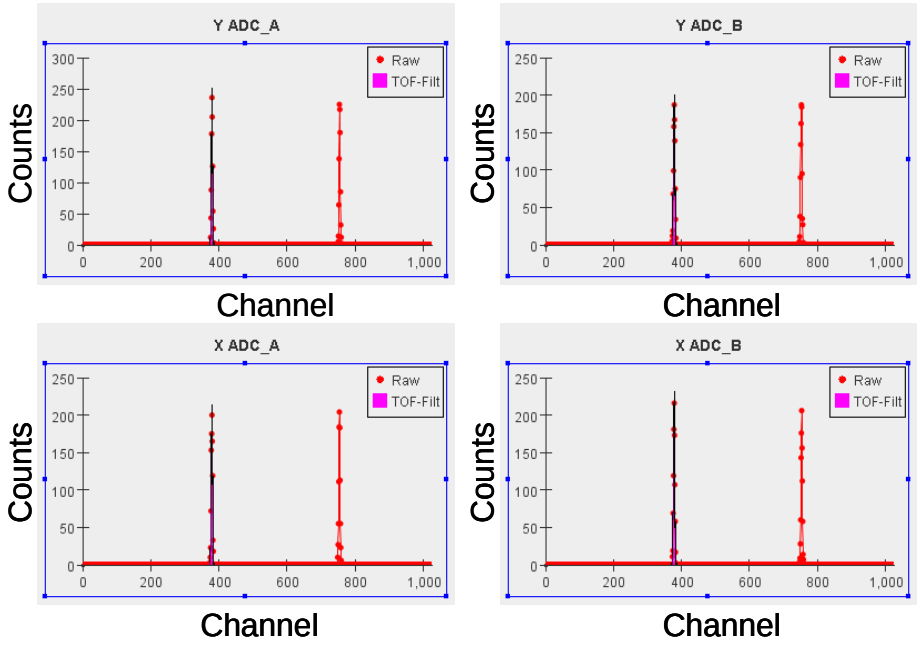

Figure 4.21: Calibrated PEM modules.

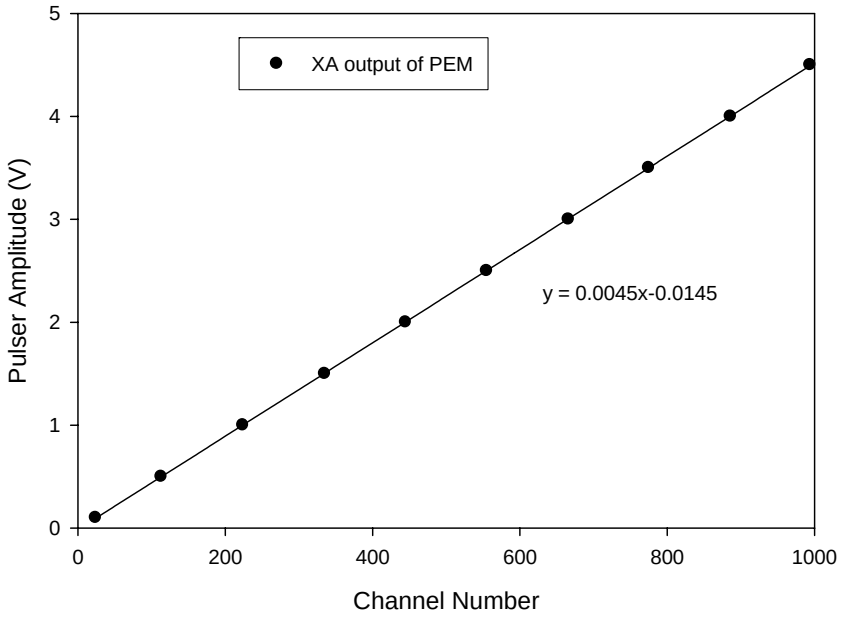

Figure 4.22: Pulse amplitude versus channel number for the XA output of the PEM.

Chapter 5 Detector testing at the NCSU PULSTAR reactor

5.1 The Neutron Powder Diffractometer at the NCSU PULSTAR Reactor

Extensive testing of both prototype 1 and prototype 2 detectors have been completed at the neutron powder diffractometer facility at the NCSU PULSTAR reactor and the National Institute of Standards and Technology [37]. The reactor became operational in 1972 and is the fourth to be operated at North Carolina State University. The reactor can operate at 1 MWth with water acting as both the coolant and moderator at a temperature of 105°F. The reactor is fueled with Uranium dioxide pin-type fuel with 4% enrichment. There are a total of 6 Beam Tubes (BTs) positioned around the core as shown in Fig. 5.1. Due to the design of the reactor, the thermal flux peaks near the edges of the core and the thermal flux at the core face is $1\times10^{13}\ \frac{neutrons}{cm^2}$. The neutron powder diffractometer has been installed at BT4 and the layout of the instrument is shown in Fig. 5.1.

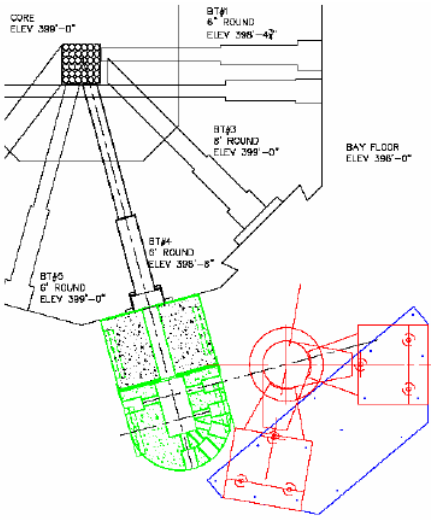

Figure 5.1: Layout of the powder neutron diffractometer at NCSU [38].

All detector tests were completed using the beam exit slit at the diffractometer. Neutrons exiting the core are collimated and a 3-inch thick sapphire filter filters the fast

neutrons out of the beam. The diffractometer beam is then produced by a silicon bent perfect crystal focusing monochromator which is optimized for a neutron wavelength of 1.478 A.

Testing of the detectors would be best in a uniform field of neutrons. However, due to the low efficiencies of the two detector prototypes, both detectors had to be placed directly in the beam. For all detector tests, the bias voltage board has been placed outside of the detector housing. This allows for easy control of the various voltages and fields in the detector and makes it possible to monitor the current across each of the components in the detector. Fig. 5.2 shows the typical experiment setup for the GEM neutron detector prototypes at the NCSU PULSTAR reactor.

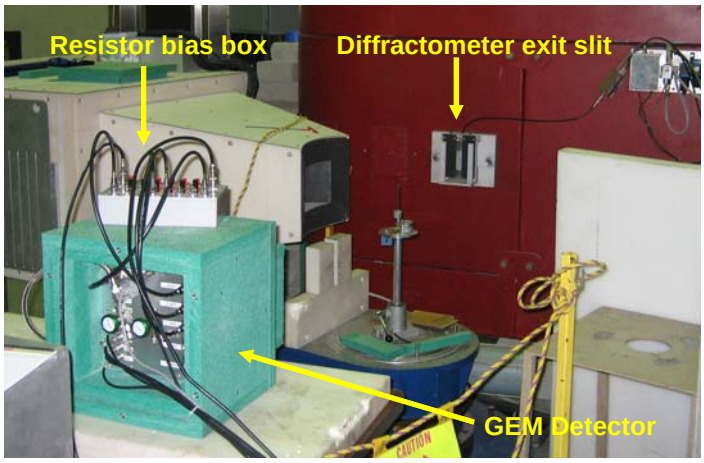

Figure 5.2: GEM detector experiment setup

5.2 Measurements with the Detectors

Several different measurements have been taken for each detector. Two-dimensional maps of the neutron flux at the face of the detector, pulse height spectra in each of the XA, XB, YA, and YB sides of the readout board, the total pulse height spectrum, and the detector efficiency have all been measured.

The total detection efficiency of a neutron detector is given by:

$$\varepsilon = \varepsilon_{ref} \frac{I_{\det}}{I_{ref}} \tag{5.1}$$

where ε_{ref} is the detection efficiency of a known reference detector and I is the measured intensity for either the reference or prototype detector. The reference detector used in the following measurements was a ^{3}He proportional tube.

5.3 Prototype 1 Testing

Tests of the prototype 1 detector demonstrated the essential elements of detector operation. The tests were completed with a 1 cm diameter circular aperture placed at the exit slit. The bias was set at -1900 V for V_1, 900 V for V_2, the TOF pulse was set to 50 Hz, the time window for coincident events was set at 1 μs, and the total counting time was 1800 seconds. The pulse height spectra for the XA, XB, YA, and YB outputs of the PEMs are shown in Fig. 5.3. The sums of XA+XB and YA+YB are shown in Fig. 5.4. Fig. 5.5 shows the number of events as a function of the x and y positions of the detector. A 2-D plot in which the sizes of the squares represent the intensity of the neutrons at that location on the face of the detector is shown in Fig. 5.6.

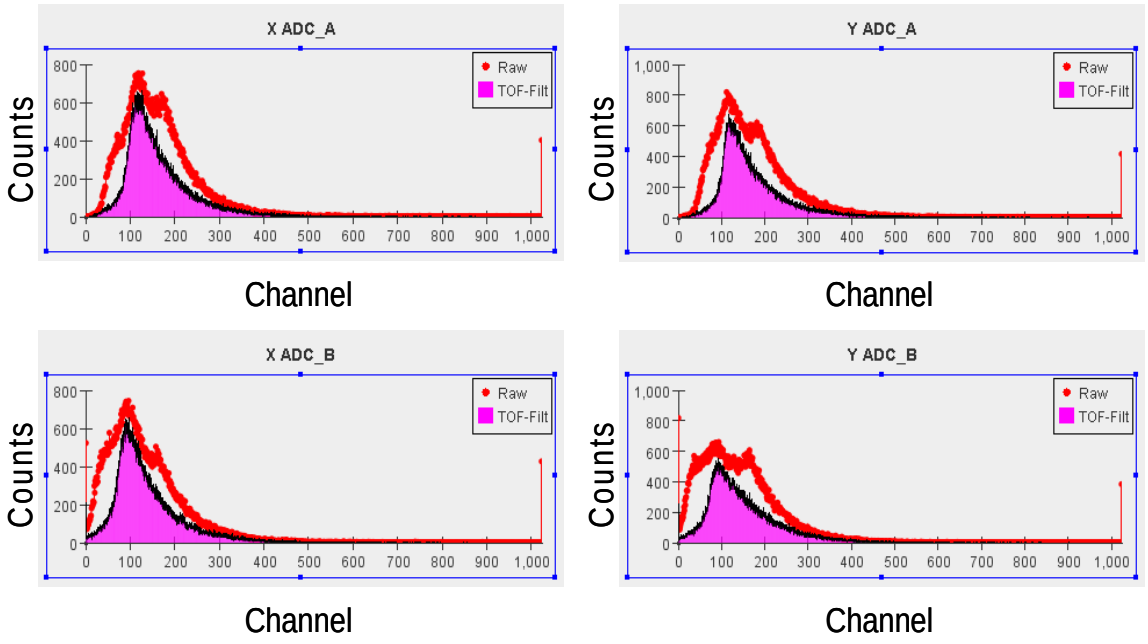

Figure 5.3: Pulse height spectra at each of the four PEM outputs.

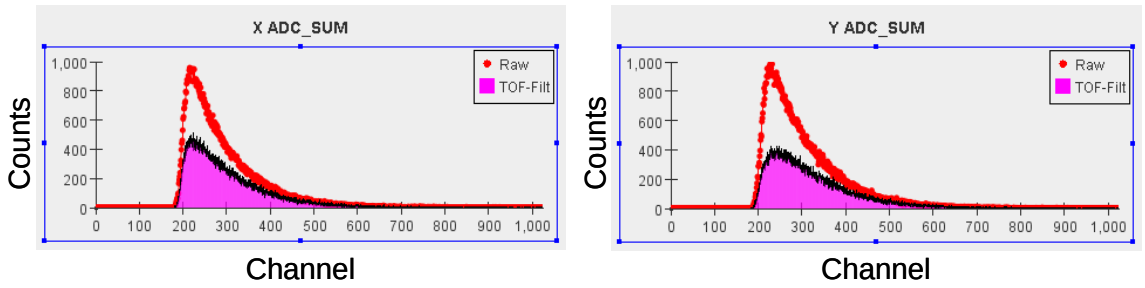

Figure 5.4: Pulse height spectra for XA+XB and YA+YB.

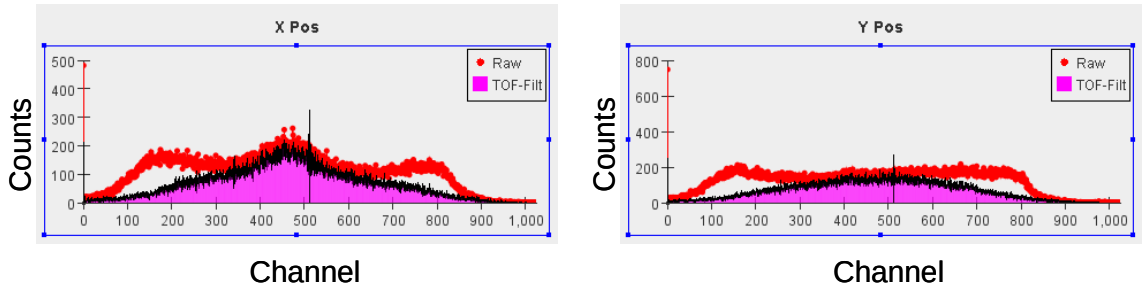

Figure 5.5: Events as a function of the x and y position.

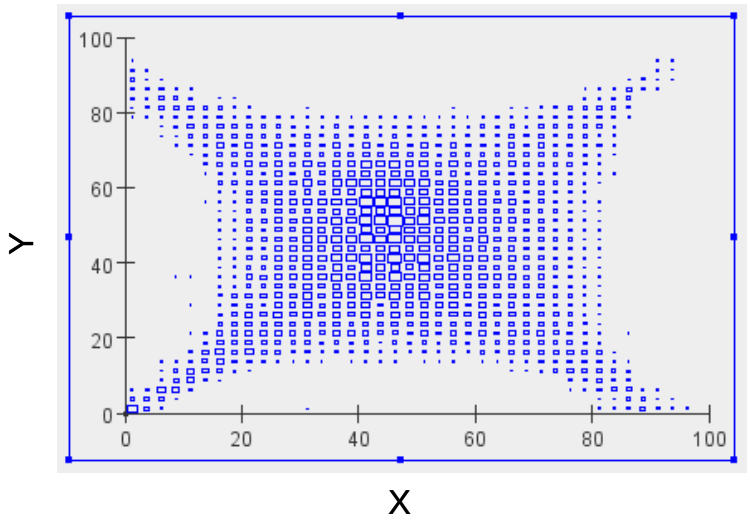

Figure 5.6: 2-D plot in which the size of the square represents the neutron intensity at that location.

A second test, under the same conditions, with a 0.1-inch thick sheet of Boral blocking the beam was also done. The statistics for both experiments are shown in table 5.1. The statistics include the raw number of events in both the x and y sides of the readout board, the x and y events which are considered to be too large, the x and y events which are not coincident in time, and the total number of coincident events (neutrons) recorded by the readout electronics.

Table 5.1: Statistics for both detector runs with and without a sheet of Boral in the beam.

Statistic	Beam open	Beam blocked
X-Raw events	110873	194776
Y-Raw events	123353	209284
X-Sum over rejects	1077	1723
Y-Sum over rejects	981	1479
X-Coincidence rejects	45392	53609
Y-Coincidence rejects	57968	68361
Coincident events	64404	139444

From the statistics above it is clear that the detector is not functioning as expected. The number of coincident events when the boral sheet blocks the beam is greater than a factor of 2 than when the beam is not blocked. One possible explanation for this is that the detector is counting the 0.48 MeV gamma rays released in the ^{10}B neutron capture reaction.

The number of coincidence rejects in both cases is large and there are different numbers of rejects in the X and Y-sides of the detector. Strong pincushion distortions are also seen in the 2-D map.

Due to these results, a test to measure the neutron detection efficiency was not completed. Since the detector contains a 5 μm thick CsI layer, which is 50x greater than the optimum layer thickness, the detector essentially behaves as a neutron/gamma ray detector. Neutron capture in the B-poly shielding leads to the emission of a 0.48 MeV gamma ray. The two above conditions make it very difficult to quantitatively state anything about the neutron detection efficiency of the detector.

5.4 Prototype 2 Testing

Due to issues described above, it was decided that instead of installing the Gd-CsI cathode in prototype 2, a Boron cathode would be used instead. This conclusion was made in order that results provided with the Boron cathode would give a better understanding of the data acquisition system and the position encoding. In this situation, the ionization due to the boron reaction products is much greater than that of a gamma ray.

The first test of detector prototype 2 was using the ^{nat}B converter screen described in the previous section. The detector was placed directly in front of the beam at a distance of 257 cm. The relative intensity of the beam in front of the 10X10 cm^2 detector area was measured with a ^{3}He detector with an effective area of 0.5X10 cm^2. The detector was moved from one side of the prototype face to the other and the measured beam profile at the detector is shown in Fig. 5.7.

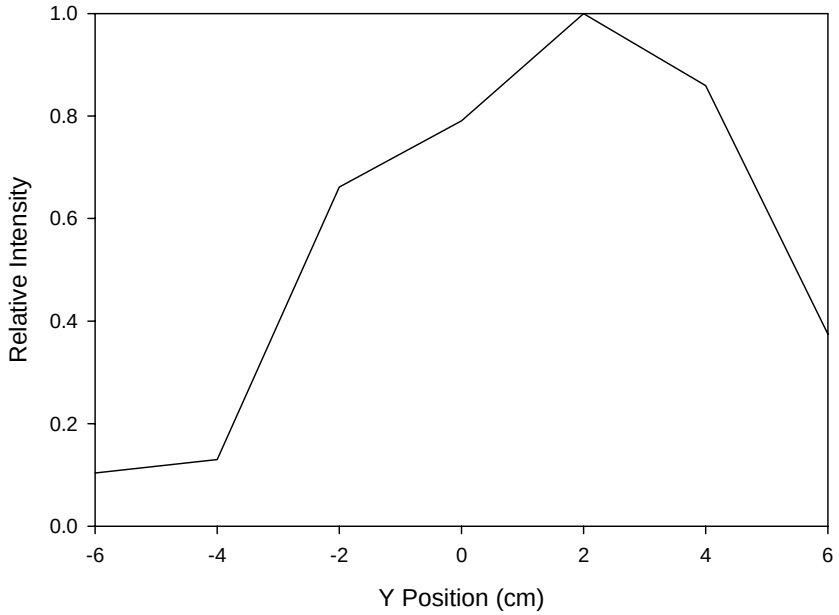

Figure 5.7: Beam profile at the detector entrance window.

The detection efficiency of the B layers when at operating voltages was estimated to be near 0.01. The efficiency of the detector when averaged over the 10X10cm^2 area was

0.0002. When compared with the desired efficiency of 10^{-5} – 10^{-7} this detector does not meet the given requirements.

A two dimensional histogram is shown in Fig. 5.8, where the colors are related to the neutron intensity at that particular spot. The statistics of the experiment are displayed on the figure. Figs. 5.8-5.11 show the typical plots printed out by the data acquisition software.

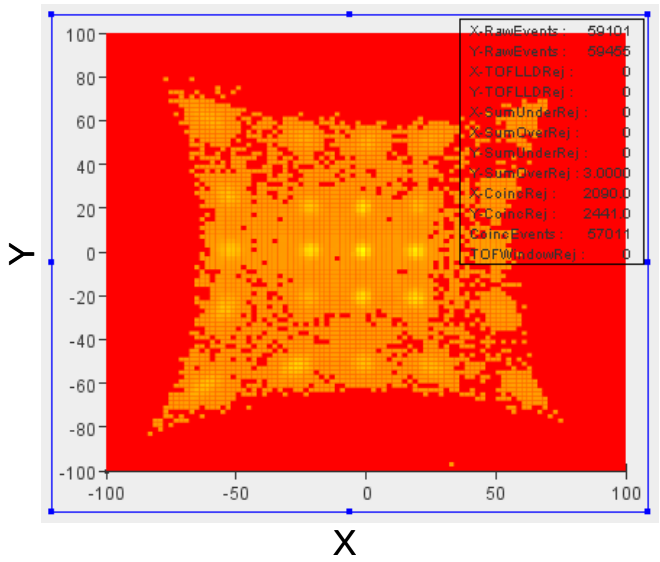

Figure 5.8: Two dimensional histogram.

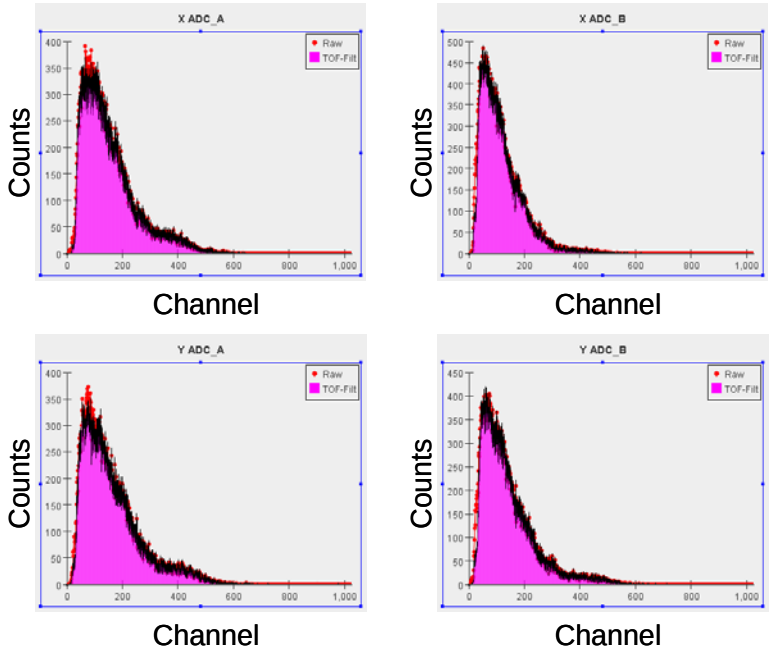

Figure 5.9: Pulse height spectra for each of the PEM outputs.

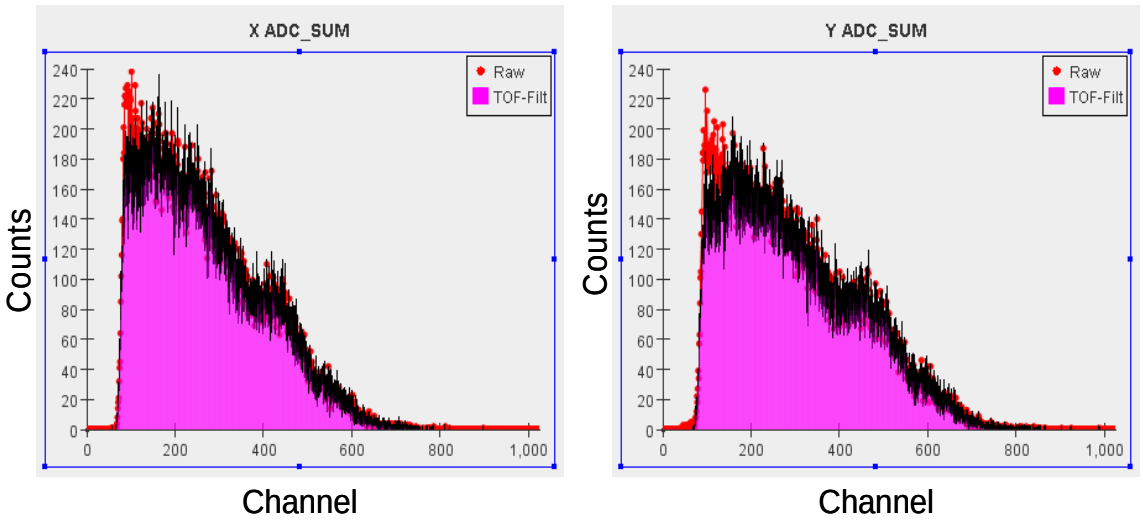

Figure 5.10: Sum pulse height spectra.

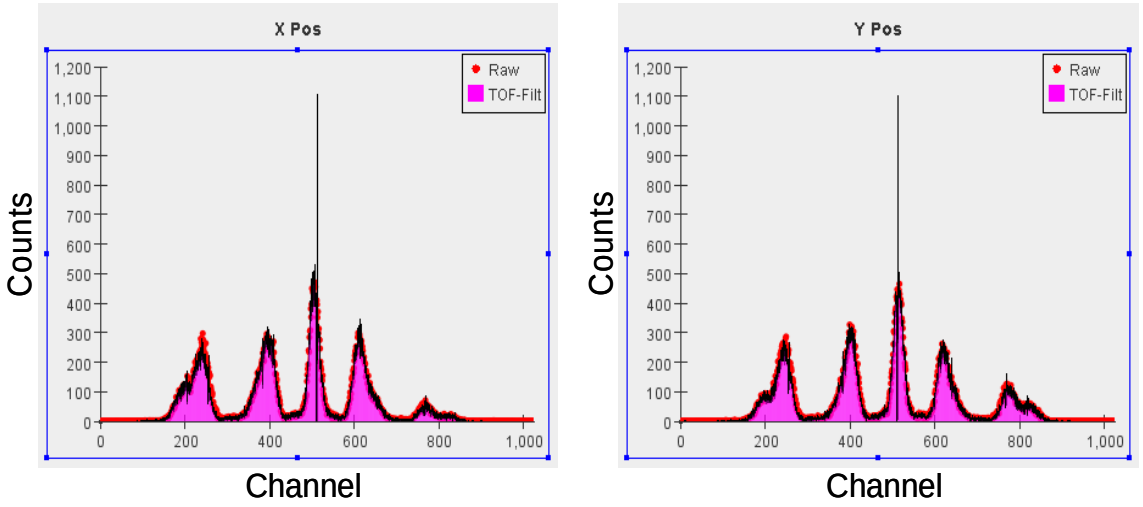

Figure 5.11: X and Y-position data for the detector runs.

Comparing this data to the experiments done with detector prototype 1, the results are quite different. Coincident rejected events are much lower in both the X and Y sides of the detector. The pincushion distortion is still apparent; however it is possible to see the 5X5 array of dots. The asymmetries in the 2-D plot can be attributed to the beam profile shown in Fig. 5.7. The intensity of the spots will also vary with the amount of Boron deposited at each location. Since the spots were dropped in place, the thickness of each spot may vary. The results also show that counts tend to pile up in the center (Fig. 5.11) of the detector even though the beam is more intense off axis of the detector.

Fig. 5.12 shows the total pulse height spectrum for the 4 μm thick ^{nat}B cathode. The pulse height spectrum shows the expected characteristics when compared with pulse height spectrum for various layer thicknesses of ^{10}B as seen in Fig. 5.13. The two flat plateaus correspond to the 0.84 MeV ^{7}Li nucleus and the 1.47 MeV α particle released 94% of the time. The detector suffers greatly from the wall effect. The small tail in the higher channels corresponds to the 1.78 MeV α particle released 6% of the time.

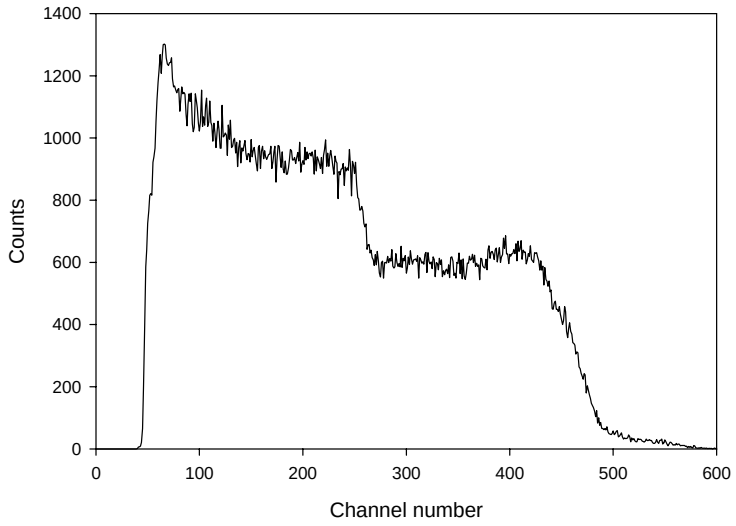

Figure 5.12: Pulse height spectrum for the prototype 2 detector with 4 μm thick ^{nat}B cathode.

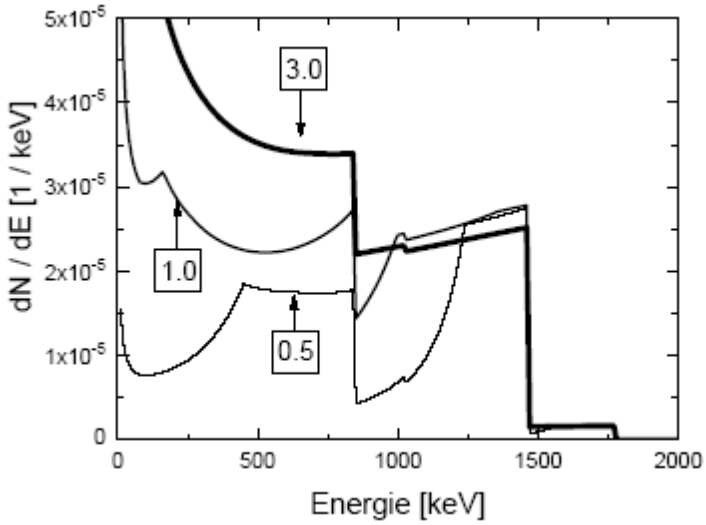

Figure 5.13: Pulse height spectra from ^{10}B converters of various thickness [39].

The effect of choosing the incorrect voltage settings is shown in Fig. 5.14. When comparing this to Fig. 5.12, the resolution of the spectrum is lost. The correct fields and voltages for prototype 2 were chosen based on the resolution of the pulse height spectrum.

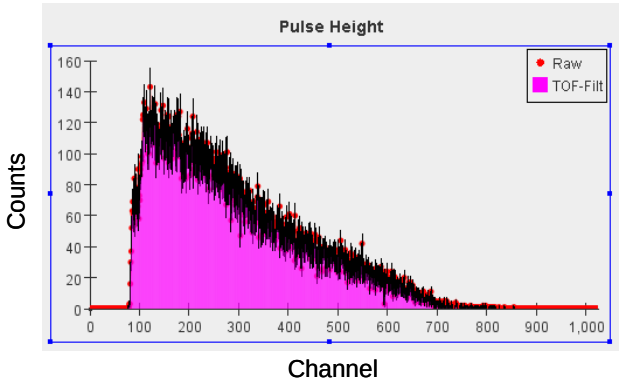

Figure 5.14: Pulse height spectrum with voltages at -2163 V and 800 V.

The second tests of prototype 2 involved the cathode screen with 1000 A thick evaporated ^{10}B. The detector was placed 191 cm from the diffractometer exit slit and the profile is shown in Fig. 5.15 as measured with the ^{3}He detector.

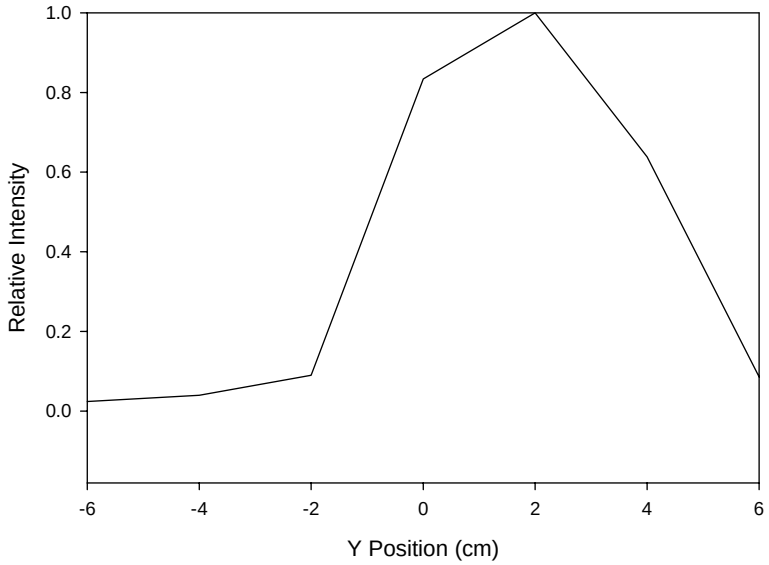

Figure 5.15: The profile of the beam at the detector opening.

The detection efficiency of the ^{10}B was estimated to be 0.007. When averaged over the entire area of the detector, the efficiency was 0.0001. Comparing this to the desired

requirements at the SNS, the efficiency is still at least a factor of 10 to high. The typical plots from the data acquisition software are shown in Figs. 5.16-5.20.

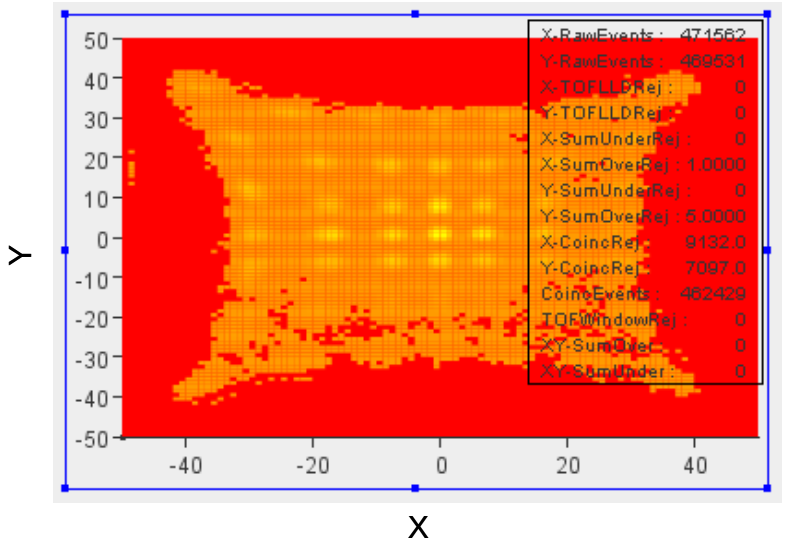

Figure 5.16: 2-D plots for detector with 1000 A thick ^{10}B dots.

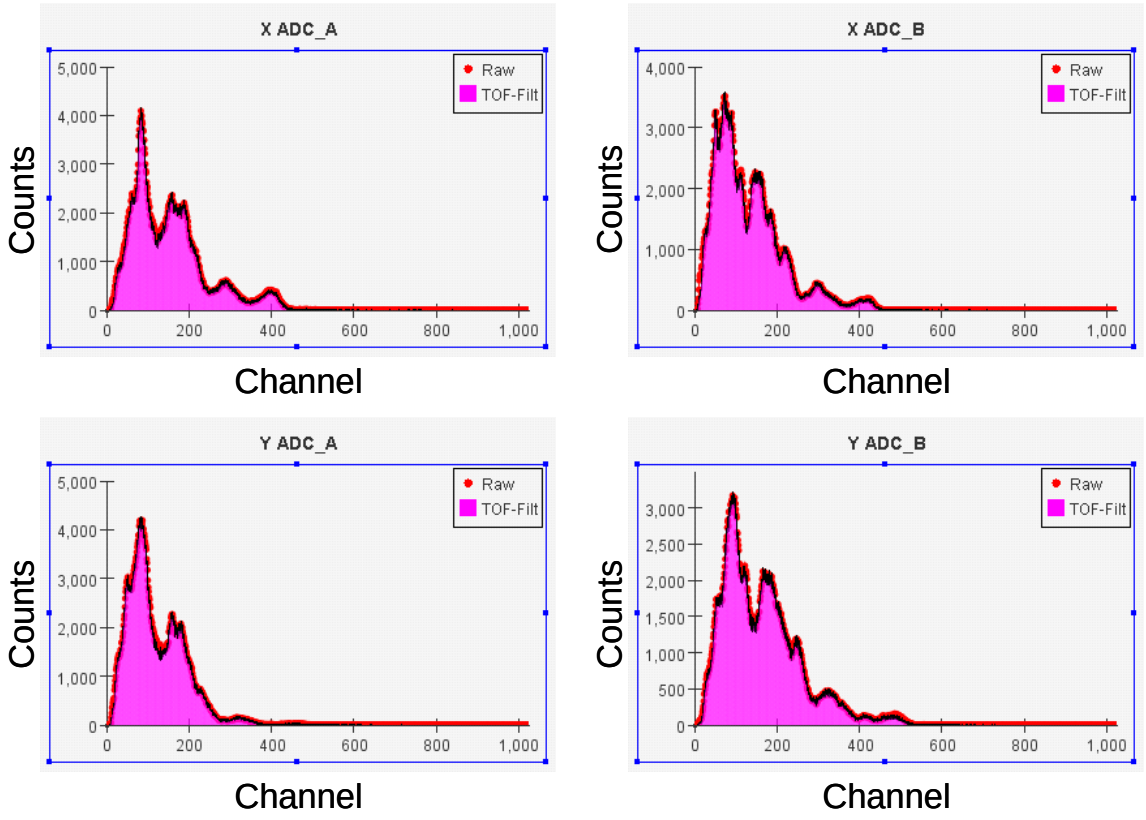

Figure 5.17: Pulse height spectra for detector using cathode with 1000 A thick ^{10}B dots.

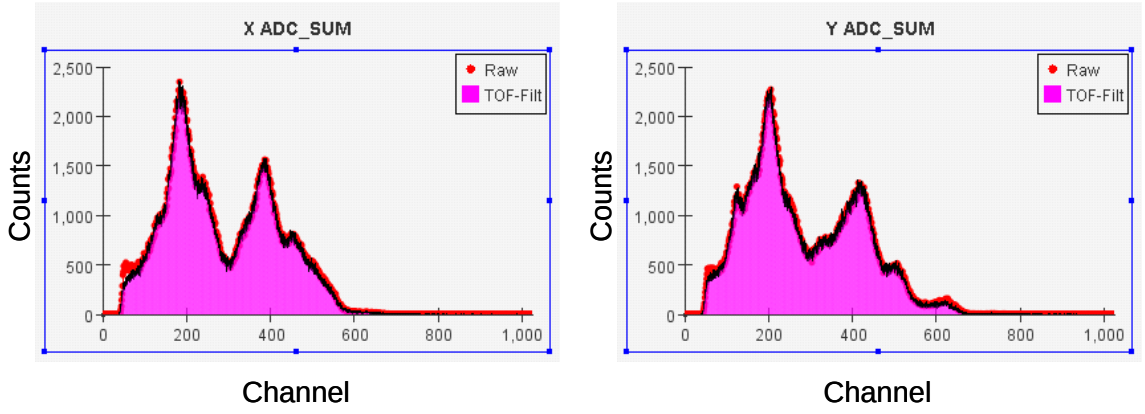

Figure 5.18: Sum spectra for cathode with 1000 A thick ^{10}B dots.

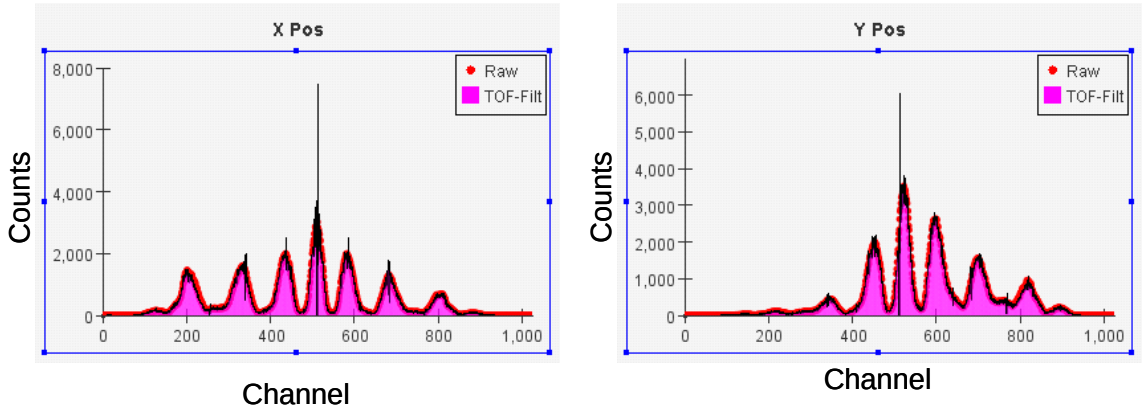

Figure 5.19: Position plots for detector with 1000 A thick ^{10}B dots.

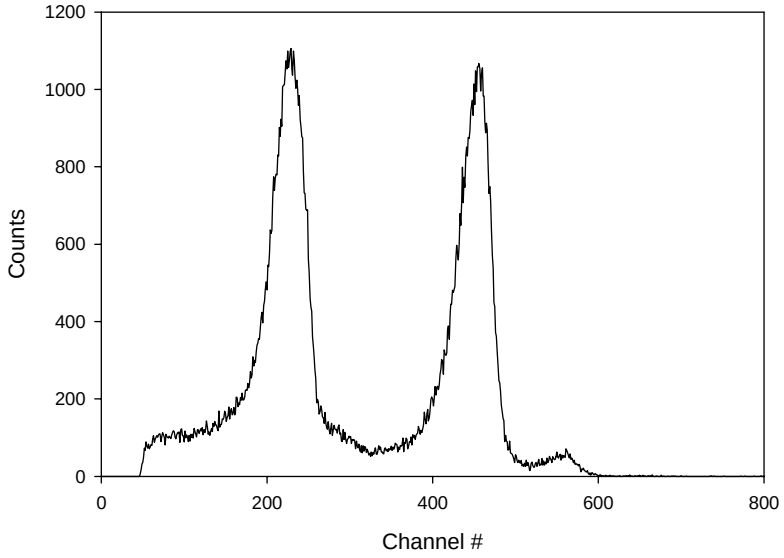

Figure 5.20: Pulse height spectra for detector with 1000 A thick ^{10}B dots.

Tests of the 1000 A ^{10}B produced similar results as with the 5 μm ^{nat}B converter. However, the major difference between the two is seen in Fig. 5.20. Full energy peaks for the 0.84 MeV ^{7}Li nucleus and the 1.47 MeV α particle released 94% of the time are easily observable. Contributions from the 1.78 MeV α particle and 1.02 MeV ^{7}Li released 6% of the time are also apparent. This difference in the pulse height spectrum is attributed to the fact that the reaction products do not suffer as much energy loss traversing the thickness of the Boron as seen in Fig. 5.12

Chapter 6 Conclusions and future work

6.1 Conclusions

The goal of this work was to simulate, build, and test a GEM neutron detector as a possible candidate for neutron scattering applications at the next generation neutron sources. Two different possible detector designs arose from the work during this project. Prototype 1 was a detector with a ^{nat}Gd/CsI converter sandwich and prototype 2 contained a B converter screen to convert the neutron to an electric signal.

The possibility of using ^{nat}Gd coated with CsI was extensively simulated in this project. Monte Carlo simulations were completed in order to find the thickness, which yielded the most number of secondary electrons for single and multi-module cases. Both differential and integral characteristics, such as the electron escape probability; the average number of low energy electrons released from the converter, and the efficiency of secondary electron production, of various setups were calculated. Testing of the prototype 1 detector showed that the detector exhibited the general characteristics of a neutron detector. However, these tests produced results, which were difficult to interpret, possibly due to the gamma sensitivity of the detector. The thickness of the CsI was 50 times greater than the layer thickness, which provided the optimum secondary electron yield.

In response to the experimental problems with prototype 1, several different Boron converter cathodes were installed and tested in prototype 2. These tests produced a functioning neutron detector in which meaningful data, such as detector efficiencies, 2-D position spectra, and pulse height spectra, could be collected. A low efficiency beam monitor for neutron scattering instruments using Boron as the neutron converter is a definite possibility.

6.2 Future Work

The results of the experiments and simulations discussed throughout this work lead to several different options for future work, which will be discussed below.

- Tests for gamma sensitivity on a neutron detector, which employs the optimum thickness of the Gd/CsI converter.
- The construction of a detector, which employs a double-sided converter foil and uses the multiple module concepts discussed previously.
- Simulations incorporating ^{157}Gd as oppose to ^{nat}Gd.
- The possibility of building a multiple module detector using solely Boron instead of the Gd/CsI sandwich.
- Tests of the detector prototypes at a pulsed neutron source, such as the SNS.
- The construction of a Boron converter foil with thinner layers to meet the 10^{-5} – 10^{-7} requirements for a beam monitor at the SNS.
- Install and take measurements with the resistive anode.

Along with all of these tests, comes design and construction of new detector electronics and readout methods, which will be adequate for neutron scattering applications at the next generation neutron sources.

References

[1] R. Pynn, "Neutron Scattering: A Primer", Los Alamos Science (1990).

[2] Why Build SNS? http://www.sns.gov/aboutsns/why_build.shtml.

[3] B. Gebauer, *Nucl. Instr. and Meth. A* **535** (2004), p. 65.

[4] G. Knoll, "Radiation Detection and Measurement", Third Edition. Ann Arbor, Michigan: John Wiley & Sons, Inc., 2000.

[5] S. Masaoka, et al., *Nucl. Instr. and Meth. A* **513** (2003), p. 538.

[6] ILL, http://www.ill.fr/.

[7] C. Schulz, Entwicklung eines neuartigen Niederdruck-Detektors mit hoher Orts- und Flugzeitauflösung zum Nachweis thermischer Neutronen, Ph.D. Dissertation, FU Berlin, 2000.

[8] N. Tsoulfandidis, "Measurement of Detection and Radiation", First Edition. Hemisphere Publishing Corporation, 1983.

[9] R. Berliner, et al., "Hardware and Software System Design for High Resolution Linear Position Sensitive Proportional Counter Detector Arrays", Proceedings of the International Workshop on Data Acquisition Systems for Neutron Experimental Facilities, Frank Laboratory of Neutron Physics, Join Institute for Nuclear Research, 1997.

[10] J. Turner, "Atoms, Radiation, and Radiation Protection", Second Edition. WILEY-VCH Verlag GmbH & Co. KGaA, 2004.

[11] R. Cooper, *Nucl. Instr. and Meth. A* **529** (2004), p. 394.

[12] Magnetism Reflectometer, http://www.sns.gov/instrument_systems/beamline_04a_mr/.

[13] Liquids Reflectometer, http://www.sns.gov/users/instrument_systems/instruments/elastic/liquid.shtml.

[14] F. Sauli, *Nucl. Instr. and Meth. A* **386** (1997), p. 531.

[15] B. Gebauer, *Nucl. Instr. and Meth. A* **392** (1997), p. 68.

[16] R. Berliner, Bull. Am. Phys. Soc., K1.171, Montreal, Canada, 2004.

[17] A. Breskin, *Nucl. Instr. and Meth. A* **367** (1995), p. 326.

[18] V. Dagendorf, et al., *Nucl. Instr. and Meth. A* **350** (1994), p. 503.

[19] A. Bressan, et al., *Nucl. Instr. and Meth. A* **424** (1999), p. 321.

[20] A. Bressan, et al., *Nucl. Instr. and Meth. A* **425** (1999), p. 254.

[21] GAS DETECTORS DEVELOPMENT GROUP, http://gdd.web.cern.ch/GDD/.

[22] R. Berliner, "A GEM of a Neutron Detector", DOE SBIR Phase-II proposal, 2004.

[23] M. Lampton and C. Carlson, *Rev. Sci. Instrum.* **50** (1979), p. 1093.

[24] F. Salvat, J.M. Fernandex-Varea, E. Acosta, J. Sempau, Workshop Proceedings, Issyles-Moulineaux, Frace, 2003.

[25] D.D. DiJulio, A.I. Hawari, and R. Berliner, "A Gd-Based Gaseous Electron Multiplier Detector for Neutron Scattering Applications," *Nucl. Instr. and Meth.* (2007), in press.

[26] A. Gibrekhterman, A. Akkerman, A. Breskin, R. Chechik, *J. Appl. Phys.* **76** (1994), p. 1676.

[27] A. Akkerman, A. Gibrekhterman, A. Breskin, R. Chechik, *J. Appl. Phys.* **72** (1992), p. 5429.

[28] A. Gibrekhterman, A. Akkerman, A. Breskin, R. Chechik, *Phys.* **74** (1993), p. 7506.

[29] R. Berliner, private communication.

[30] C. Richter, et al., *Nucl. Instr. and Meth. A* **478** (2002), p. 538.

[31] P.R.B. Marinho, G.P. Guedes, A.F. Barbosa, P.C.M.A. Farias, *Radiation Measurements.* **39** (2005), p. 515.

[32] S.M.A.R.T Laboratory, Manhattan, KS, 785-532-5610, http://www.mne.ksu.edu/research/centers/SMARTlab/.

[33] CASCADE – neutron detectors, http://www.physi.uni-heidelberg.de/physi/cascade/konzept.html.

[34] Tech Etch, Inc, Plymouth, MA, 508-747-0300, http://www.tech-etch.com/.

[35] Instrumentation Associates, Durham, NC, 919-765-0034.

[36] LeCroy Corporation, Chestnut Ride, NY, 800-553-2769, http://www.lecroy.com/.

[37] R. Berliner, D. DiJulio, and A.I. Hawari, "A GEM of a Neutron Detector". American Conference on Neutron Scattering, St. Charles IL, June 18-22 2006.

[38] R. Berliner, "PNPD: A High Performance Neutron Powder Diffractometer at a Low Intensity Source", ORNL Seminar, 2007.

[39] M. Klein, Experimente zur Quantenmechanik mit ultrakalten Neutronen und Entwicklung eines neuen Detektors zum ortsaufgelösten Nachweis von thermischen Neutronen auf groBen Flächen , Ph.D. Dissertation, Ruprecht-Karls-Universität Heidelberg, 2000.

Appendices

Appendix A

A typical example of a PENELOPE input file for the modified PENCYL program for the double-sided converter screen is given by the following text. The first six columns are reserved for the input line keyword while the numerical data starts at the 8th column. The program ignores the comments in the square brackets. Refer to reference [24] for a detailed description of the entire input file and how to choose the simulation parameters.

```
TITLE  DB EXP GEM Geometry
GSTART Gd backed with CsI
LAYER        -1.1e-03    -1.05e-03
CYLIND        3  0  1
LAYER        -1.05e-03   -7.5e-04
CYLIND        2  0  1
LAYER        -7.5e-04    0
CYLIND        1  0  1
LAYER         0          3.0e-04
CYLIND        2  0  1
LAYER        3.0e-04     3.5e-04
CYLIND        3  0  1
GEND
SKPAR  1       [Primary particles: 1=electron, 2=photon, 3=positron]
SPECTR    2.9000E+04    0.299
SPECTR    3.0000E+04    1.00E-08
SPECTR    3.1000E+04    1.00E-08
SPECTR    3.2000E+04    1.00E-08
SPECTR    3.3000E+04    1.00E-08
SPECTR    3.4000E+04    1.00E-08
SPECTR    3.5000E+04    1.00E-08
SPECTR    3.6000E+04    1.00E-08
SPECTR    3.7000E+04    1.00E-08
SPECTR    3.8000E+04    1.00E-08
SPECTR    3.9000E+04    1.00E-08
SPECTR    4.0000E+04    1.00E-08
SPECTR    4.1000E+04    1.00E-08
SPECTR    4.2000E+04    1.00E-08
SPECTR    4.3000E+04    1.00E-08
SPECTR    4.4000E+04    1.00E-08
SPECTR    4.5000E+04    1.00E-08
SPECTR    4.6000E+04    1.00E-08
SPECTR    4.7000E+04    1.00E-08
SPECTR    4.8000E+04    1.00E-08
```

SPECTR	4.9000E+04	1.00E-08
SPECTR	5.0000E+04	1.00E-08
SPECTR	5.1000E+04	1.00E-08
SPECTR	5.2000E+04	1.00E-08
SPECTR	5.3000E+04	1.00E-08
SPECTR	5.4000E+04	1.00E-08
SPECTR	5.5000E+04	1.00E-08
SPECTR	5.6000E+04	1.00E-08
SPECTR	5.7000E+04	1.00E-08
SPECTR	5.8000E+04	1.00E-08
SPECTR	5.9000E+04	1.00E-08
SPECTR	6.0000E+04	1.00E-08
SPECTR	6.1000E+04	1.00E-08
SPECTR	6.2000E+04	1.00E-08
SPECTR	6.3000E+04	1.00E-08
SPECTR	6.4000E+04	1.00E-08
SPECTR	6.5000E+04	1.00E-08
SPECTR	6.6000E+04	1.00E-08
SPECTR	6.7000E+04	1.00E-08
SPECTR	6.8000E+04	1.00E-08
SPECTR	6.9000E+04	1.00E-08
SPECTR	7.0000E+04	1.00E-08
SPECTR	7.1000E+04	4.98E-01
SPECTR	7.2000E+04	1.00E-08
SPECTR	7.3000E+04	1.00E-08
SPECTR	7.4000E+04	1.00E-08
SPECTR	7.5000E+04	1.00E-08
SPECTR	7.6000E+04	1.00E-08
SPECTR	7.7000E+04	1.00E-08
SPECTR	7.8000E+04	1.22E-01
SPECTR	7.9000E+04	1.00E-08
SPECTR	8.0000E+04	1.00E-08
SPECTR	8.1000E+04	1.00E-08
SPECTR	8.2000E+04	1.00E-08
SPECTR	8.3000E+04	1.00E-08
SPECTR	8.4000E+04	1.00E-08
SPECTR	8.5000E+04	1.00E-08
SPECTR	8.6000E+04	1.00E-08
SPECTR	8.7000E+04	1.00E-08
SPECTR	8.8000E+04	1.00E-08
SPECTR	8.9000E+04	1.00E-08
SPECTR	9.0000E+04	1.00E-08
SPECTR	9.1000E+04	1.00E-08
SPECTR	9.2000E+04	1.00E-08
SPECTR	9.3000E+04	1.00E-08
SPECTR	9.4000E+04	1.00E-08

SPECTR	9.5000E+04	1.00E-08
SPECTR	9.6000E+04	1.00E-08
SPECTR	9.7000E+04	1.00E-08
SPECTR	9.8000E+04	1.00E-08
SPECTR	9.9000E+04	1.00E-08
SPECTR	1.0000E+05	1.00E-08
SPECTR	1.0100E+05	1.00E-08
SPECTR	1.0200E+05	1.00E-08
SPECTR	1.0300E+05	1.00E-08
SPECTR	1.0400E+05	1.00E-08
SPECTR	1.0500E+05	1.00E-08
SPECTR	1.0600E+05	1.00E-08
SPECTR	1.0700E+05	1.00E-08
SPECTR	1.0800E+05	1.00E-08
SPECTR	1.0900E+05	1.00E-08
SPECTR	1.1000E+05	1.00E-08
SPECTR	1.1100E+05	1.00E-08
SPECTR	1.1200E+05	1.00E-08
SPECTR	1.1300E+05	1.00E-08
SPECTR	1.1400E+05	1.00E-08
SPECTR	1.1500E+05	1.00E-08
SPECTR	1.1600E+05	1.00E-08
SPECTR	1.1700E+05	1.00E-08
SPECTR	1.1800E+05	1.00E-08
SPECTR	1.1900E+05	1.00E-08
SPECTR	1.2000E+05	1.00E-08
SPECTR	1.2100E+05	1.00E-08
SPECTR	1.2200E+05	1.00E-08
SPECTR	1.2300E+05	1.00E-08
SPECTR	1.2400E+05	1.00E-08
SPECTR	1.2500E+05	1.00E-08
SPECTR	1.2600E+05	1.00E-08
SPECTR	1.2700E+05	1.00E-08
SPECTR	1.2800E+05	1.00E-08
SPECTR	1.2900E+05	1.00E-08
SPECTR	1.3000E+05	1.00E-08
SPECTR	1.3100E+05	5.64E-02
SPECTR	1.3200E+05	1.00E-08
SPECTR	1.3300E+05	1.00E-08
SPECTR	1.3400E+05	1.00E-08
SPECTR	1.3500E+05	1.00E-08
SPECTR	1.3600E+05	1.00E-08
SPECTR	1.3700E+05	1.00E-08
SPECTR	1.3800E+05	1.00E-08
SPECTR	1.3900E+05	1.00E-08
SPECTR	1.4000E+05	1.00E-08

```
SPECTR    1.4100E+05    1.00E-08
SPECTR    1.4200E+05    1.00E-08
SPECTR    1.4300E+05    1.00E-08
SPECTR    1.4400E+05    1.00E-08
SPECTR    1.4500E+05    1.00E-08
SPECTR    1.4600E+05    1.00E-08
SPECTR    1.4700E+05    1.00E-08
SPECTR    1.4800E+05    1.00E-08
SPECTR    1.4900E+05    1.00E-08
SPECTR    1.5000E+05    1.00E-08
SPECTR    1.5100E+05    1.00E-08
SPECTR    1.5200E+05    1.00E-08
SPECTR    1.5300E+05    1.00E-08
SPECTR    1.5400E+05    1.00E-08
SPECTR    1.5500E+05    1.00E-08
SPECTR    1.5600E+05    1.00E-08
SPECTR    1.5700E+05    1.00E-08
SPECTR    1.5800E+05    1.00E-08
SPECTR    1.5900E+05    1.00E-08
SPECTR    1.6000E+05    1.00E-08
SPECTR    1.6100E+05    1.00E-08
SPECTR    1.6200E+05    1.00E-08
SPECTR    1.6300E+05    1.00E-08
SPECTR    1.6400E+05    1.00E-08
SPECTR    1.6500E+05    1.00E-08
SPECTR    1.6600E+05    1.00E-08
SPECTR    1.6700E+05    1.00E-08
SPECTR    1.6800E+05    1.00E-08
SPECTR    1.6900E+05    1.00E-08
SPECTR    1.7000E+05    1.00E-08
SPECTR    1.7100E+05    1.00E-08
SPECTR    1.7200E+05    1.00E-08
SPECTR    1.7300E+05    2.02E-02
SPECTR    1.7400E+05    1.00E-08
SPECTR    1.7500E+05    1.00E-08
SPECTR    1.7600E+05    1.00E-08
SPECTR    1.7700E+05    1.00E-08
SPECTR    1.7800E+05    1.00E-08
SPECTR    1.7900E+05    1.00E-08
SPECTR    1.8000E+05    5.25E-03
SPECTR    1.8100E+05    0.00E+00
SEXTND 2 4 1 0
SDIREC 0 0
SAPERT 180
NMAT   3                  [Number of different materials, .le.10]
SIMPAR 1 100 100 100 0 0 0 11   [M,EABS,C1,C2,WCC,WCR]
```

```
SIMPAR 2 100 100 100 0 0 0 11   [M.EABS,C1,C2,WCC,WCR]
SIMPAR 3 100 100 100 0 0 0 11   [M.EABS,C1,C2,WCC,WCR]
PFNAME kap.mat              [Material definition file, 18 characters]
NSIMSH 2147483647           [Desired number of simulated showers, max=2**31-1]
TIME   3600                 [Allotted simulation time, in sec]
```

The lines between the keywords GSTART and GEND designate the geometry definition list. The line LAYER represents the z-coordinates in which that layers thickness is defined. CYLIND defines the type of material, the inner radius, and the outer radius of the cylinder.

The lines labeled SPECTR define the Gd energy spectrum, the first entry being the energy and the second energy the total probability for that entry.

SEXTND defines an extended source in which the first and second entries correspond to the layers in which the source extends. In this case, the source is exponential and extends layers 2 and 4, which are the Gd layers. The 3rd entry corresponds to the cylinder in which the source exists in; this label is printed out by the geometry output report. The 4th is the relative activity concentration of the source.

SDIREC defines the beam axis direction in angles. The first entry is the angle theta and the second entry is the angle phi. SAPERT defines the angular aperture (SALPHA) of the source beam, in degrees. A cone of (semi-) aperture SALPHA, with a central axis in the direction, theta, phi, defines the region in which the initial direction of the particles is sampled from.

NMAT is the number of different materials used in the simulations. SIMPAR controls the simulations parameters in each of the materials. The first three entries are the absorption energies, which must be greater than 100 eV. The following two entries are the elastic

scattering parameters. The final two entries are the cutoff energy losses for inelastic collisions and bremsstrahlung emission.

PFNAME is the label given to the material data file that is used in the simulations. NSIMSH is the total desired number of showers to be run. TIME is the allotted simulation time in seconds.